



On the ensemble requirement of fully selective chemical looping methane partial oxidation over La-Fe-based perovskites

Jie Yang^a, Erlend Bjørgum^{b,1}, Hui Chang^a, Ka-Ke Zhu^a, Zhi-Jun Sui^a, Xing-Gui Zhou^a, Anders Holmen^b, Yi-An Zhu^{a,*}, De Chen^{b,*}

^a UNILAB, State Key Laboratory of Chemical Engineering, School of Chemical Engineering, East China University of Science and Technology, Shanghai 200237, China

^b Department of Chemical Engineering, Norwegian University of Science and Technology, NO-91, Trondheim, Norway

ARTICLE INFO

Keywords:

Perovskite
Methane partial oxidation
Surface oxygen vacancy
Methane total combustion
C-H bond activation

ABSTRACT

The dynamic nature of active sites on La-Fe-based perovskites in chemical looping methane oxidation has been studied. According to experimental observations, the reduction of the oxygen carrier is divided into three stages occurring at different active ensembles where the Fe cations are in different coordination environments. The Mars van Krevelen mechanism formulated by microkinetic analysis describes well the effect of oxygen vacancy on the catalytic performance of LaFeO₃. CO₂ is not produced by CO oxidation but rather is a primary product of methane oxidation, and the presence of surface oxygen vacancies would dramatically increase the overall energy barrier for total combustion, thus decreasing the selectivity toward CO₂. Hence, the Fe coordination environment (and hence the oxygen vacancy concentration) is the key parameter governing the catalyst selectivity, in the sense that methane oxidation can vary from total combustion on the O-rich surface to fully selective partial oxidation on the O-deficient surface.

1. Introduction

Partial oxidation of methane as a mildly exothermic reaction compared to steam and dry reforming of methane produces syngas with a suitable ratio of hydrogen and monoxide, [1] which is beneficial to subsequent F-T synthesis and other reactions to produce value-added chemical products. The chemical looping reforming (CLR) has been widely studied in methane oxidation to avoid direct contact between pure oxygen and methane [2–4]. It is generally accepted that the catalyzed redox reactions occur by the Mars van Krevelen mechanism [5] in chemical looping partial oxidation (CLPO). In the redox cycle, the methane is oxidized by lattice oxygen instead of pure oxygen, and the reduced catalyst with oxygen vacancy is regenerated by the introduction of air or oxygen. The research on CLPO is mainly focused on the catalysts and it is found that the necessary conditions for an excellent oxygen carrier include good catalytic activity for the production of CO and H₂ from the fuel and resistance to carbon deposition. Hence, reducing the CO₂/H₂O production and giving rise to production of syngas are of great importance. Many oxides such as Manganese oxides [6], cerium oxides [7,8], palladium oxides [9], Fe/Cu/Ni oxides [10–13] and perovskites

[14–16] have been extensively studied for methane oxidation in CLPO, among which perovskites have shown great promise as catalyst candidates.

Perovskites with a general formula of ABO₃, where the A- and B-site cations represent the metals at the 12- and 6-coordinated sites, respectively [17], have been intensively investigated as one of the most promising materials applied in solid oxide fuel cells (SOFCs) [18,19], catalysts and oxygen carriers in heterogeneous catalysis [20,21], oxygen separation membranes [22], and solid-state gas sensors [23]. The catalytic properties of perovskites have been comprehensively studied [24, 25], and these materials, which may accommodate various substituents and dopants to improve catalytic activity by changing the elemental composition and oxidation state [20], have been widely used for chemical looping processes [26–36]. For instance, Gong et al. [37] studied a series of La_{1-x}Ce_xFeO₃ (x = 0, 0.25, 0.5, 0.75, and 1) perovskites and found that La_{0.5}Ce_{0.5}FeO₃ with the best bulk oxygen mobility and surface reaction activity exhibits the best methane conversion, syngas selectivity, syngas yield, and redox stability. Likewise, Wang et al. [28] found that the A-site engineering in the La_{1-x}Sr_xFe_{0.8}Al_{0.2}O₃ oxides significantly tunes the oxygen capacity, which nearly triples from

* Corresponding authors.

E-mail addresses: yanzhu@ecust.edu.cn (Y.-A. Zhu), de.chen@ntnu.no (D. Chen).

¹ Present address: Equinor, Mongstad, 5954, Monstad, Norway.

1.0 mmol/g ($x = 0.1$) to 2.7 mmol/g ($x = 0.5$) with the CO selectivity kept above 94%. Moreover, a perovskite-based oxygen carrier ($\text{La}_{0.85}\text{Sr}_{0.15}\text{Fe}_{0.95}\text{Al}_{0.05}\text{O}_{3-\delta}$) was recently reported to show the ability to completely convert methane to syngas with a CO selectivity of more than 99% [29].

The LaFeO_3 perovskite has long been used as a promising catalyst for chemical looping methane partial oxidation, where the reaction is initially selective toward the formation of CO_2 and H_2O , and then the rate for total combustion decreases rapidly while the selectivity towards CO and H_2 increases [38]. Since there are different reactions involved in the chemical looping methane oxidation process, the overall kinetics is complicated, giving rise to the difficulty of investigating the mechanism. Methane oxidation pathways have been studied on iron oxides [39–41]. It was reported that in the chemical looping process CO is a primary product of methane partial oxidation rather than a secondary product of methane total combustion followed by dry and steam reforming of methane [29,31,42–44]. The latter has often been observed in the traditional methane partial oxidation reaction. Liu et al. [45] synthesized the nanoscaled iron-based oxygen carriers for chemical looping partial oxidation of methane, which shows high catalytic activity and nearly 100% CO selectivity. By using DFT calculations, they believed that the origin of such a high selectivity lies in the fact that under-coordinated lattice oxygen atoms promote Fe-O bond cleavage and CO formation. In addition, Mihai et al. [16] also proposed three types of active sites for methane oxidation on the surface where Fe atoms highly coordinated to O and vacancy sites lead to the total combustion of methane and carbon formation, respectively, while those moderately coordinated to O give rise to partial oxidation of methane. Hence, the partial oxidation of methane seems to occur on the surface with low oxygen concentration or high oxygen vacancy concentration. However, it remains elusive how the Fe and O ions can coordinatively promote partial methane oxidation and achieve high CO selectivity. Moreover, the three reaction stages on perovskites are such complex multi-dimensional dynamic reactions that their microscopic description is still not clear.

The present study is focused on unraveling the critical role of the oxygen vacancy in the activity and selectivity of methane oxidation over LaFeO_3 -based perovskites. The relationship between the temperature/weight hourly space velocity (WHSV) and activity/selectivity in methane (partial) oxidation, together with the catalytic activity of LaFeO_3 with the desired degree of reduction and re-oxidation of $\text{LaFeO}_{3-\delta}$, have been investigated through a transient kinetic study. Theoretically, DFT calculations and microkinetic analysis are carried out to probe the reaction mechanism for methane oxidation at different reaction stages and active ensembles where the Fe cations are in different coordination environments on LaFeO_3 . The geometrical structures of four active ensembles are first defined and analyzed. Then, the adsorption behaviors of the reaction intermediates and transition states as well as the kinetics of the redox reaction are examined to identify the main active ensemble and dominant reaction pathway leading to partial or total oxidation. Finally, a strategy of controlling the oxidation time of $\text{LaFeO}_{3-\delta}$ and the amount of oxygen injected to the perovskite is demonstrated to achieve 100% selectivity toward syngas.

2. Experimental and computational details

2.1. Catalyst preparation and characterization

$\text{LaFeO}_{3-\delta}$ was synthesized using the glycine-nitrate combustion method [46]. A stoichiometric amount of an aqueous cationic nitrate solution was prepared, adding glycine with glycine/nitrate molar ratio 5/9 as a complexing agent. The proportion of water in the nitrates was measured through thermogravimetric analysis, and three parallel experiments were performed for each nitrate. The thermogravimetric analysis identifies the exact number of cations in nitrate salts by heating the nitrate to 1273 K for 24 h and weighing the resulting oxides. The solution is

heated and evaporated in a glass tube until the gel is ignited and decomposed into oxides. The oxides were preheated to 1073–1173 K while falling through a vertical alumina tube, and the resulting oxide powders in 100% ethanol were ball-milled (Si_3N_4 -balls) overnight. Finally, the powders were further calcined at 1173 K for 10 h in air. The synthesized samples were then characterized by using X-ray diffraction (XRD), X-ray photoelectron spectroscopy (XPS), temperature-programmed reduction (TPR), and temperature-programmed surface reaction (TPSR), scanning electron microscope (SEM), in much the same way as that proposed in our previous work [30,38], and the detailed results of the characterization of the perovskites are given therein.

2.2. Catalytic testing

The experiments were conducted using a quartz fixed-bed micro-reactor (15 mm ID and 350 mm long) while the catalyst was fixed on a sinter and an electrical furnace was used for heating. The product composition was analyzed by an on-line GASLAB 300 mass spectrometer. Except for water, which is calculated based on the mass balance, all gas-phase components were calibrated by using a calibration gas with known composition because the water is in a small amount in the reaction. The flows of O_2/Ar and CH_4/Ar were switched to achieve a redox cycle, and among the switches, the reactor system was flushed with Ar to remove the O_2 . The total flow rate was kept at 40 mL/min in all the experiments. 10 mL/min O_2 in Ar were used for the oxidation reaction, while the CH_4 flow rate was varied from 7.2 to 16 mL/min CH_4 in Ar. Most of the experiments were performed at 1173 K, and the catalyst loading was 1.00 g for all the experiments.

2.3. DFT calculations

All spin-polarized self-consistent DFT calculations were performed using the VASP software package [47–49]. The exchange and correlation in the Kohn-Sham theory was treated with the BEEF-vdW functional [50]. The projector-augmented wave (PAW) method was employed to describe the interactions of ion cores with valence electrons [51], and by using the PAW potentials with the valence electron configurations La ($5s^2 5p^6 6s^2 5d^1$), O ($2s^2 2p^4$), and Fe ($3p^6 3d^6 4s^2$), a plane wave energy cutoff up to 600 eV was found to be essential to the convergence of the energy per atom in the system to better than 1 meV. Given the fact that standard exchange-correlation functionals suffer from excessive electron delocalization [52], an additional Hubbard-type term was applied in the rotationally invariant DFT+U method [53–55]. The used effective U (U_{eff}) values for Fe is 2.9 eV, which has been obtained by fitting the calculated energetics of formation of transition-metal oxides to available experimental data [56] and proven to be able to predict the physical and chemical properties of LaFeO_3 perovskites with reasonable accuracy, such as band gap, magnetic moment, and oxygen vacancy formation energy [56]. Sampling of the Brillouin zone was carried out with the Monkhorst-Pack method [57], and the Gaussian smearing method with a width of 0.1 eV was used to determine the partial occupancies of the orbitals. The effect of spin polarization was considered throughout the work.

The dimer method [58] was used to search for the transition states, which were then verified to have only one imaginary frequency through vibrational frequency analysis. Both the geometry optimization and transition-state search are based on a force-based conjugated-gradient method and are considered to be converged when the forces on each atom are less than $0.03 \text{ eV}/\text{\AA}$. To measure the strength of the interaction between adsorbed species and oxide surfaces, the adsorption energy (ΔE_{ads}) was calculated as

$$\Delta E_{\text{ads}} = E_{\text{adsorbate/surface}} - E_{\text{surface}} - E_{\text{adsorbate}} \quad (1)$$

where $E_{\text{adsorbate/surface}}$, E_{surface} , and $E_{\text{adsorbate}}$ are the total energies of the surface with the species adsorbed, the bare surface, and an isolated

species.

2.4. Structural models

In our previous work, the equilibrium lattice constants of LaFeO_3 were obtained by optimizing the bulk structure of the stoichiometric perovskite [59]. As the energetically most favorable and most frequently encountered surface [60–65], $\text{LaFeO}_3(001)$ is chosen to represent the catalyst surface, where DFT calculations and microkinetic analysis have been carried out on its four different terminations. The $\text{LaFeO}_3(001)$ surface with a FeO_2 termination is represented as a twelve-layer (three-unit-layer) slab with a $p(1 \times 1)$ cell, as shown schematically in Fig. 1a. The bottom unit layer of the slab was kept fixed at their crystal lattice positions while the adsorbates and the remainder of the slab were

allowed to fully relax. The adjacent slabs are separated by a vacuum spacing of 12 \AA along the surface normal to eliminate periodic interactions. For such a model, a Γ -centered $4 \times 4 \times 1$ grid proves to be sufficient to converge the total energy per atom in the system to within 1 meV . As a first test of our methods, a $p(2 \times 2)$ supercell with the same FeO_2 termination has also been constructed to explore the energy dependence on the cell size (see Table S1). It was found that increasing the cell size has a negligible effect on the calculated adsorption energy of H at the Fe site, suggesting that the $p(1 \times 1)$ cell can give a reasonably reliable description of the energetics of bond formation on the $\text{LaFeO}_3(001)$ surface. Dipole correction was not applied in this work because the dipole moment can only change the calculated adsorption energies by less than 0.08 eV (see Table S2).

In addition, three other terminations with different surface oxygen

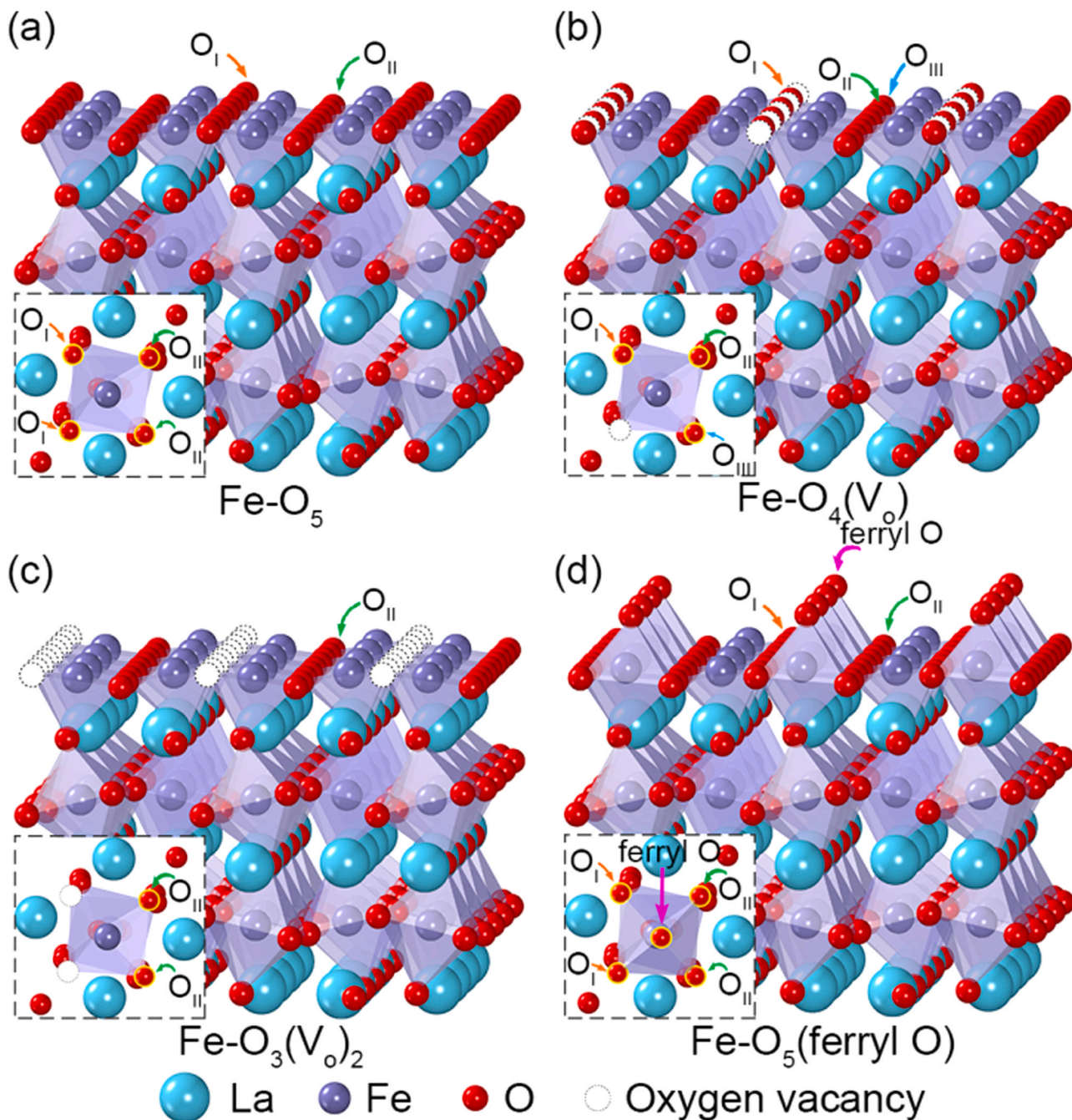


Fig. 1. Schematic representations of local structures around Fe on $\text{LaFeO}_3(001)$, with Fe in the (a) Fe-O_5 , (b) $\text{Fe-O}_4(\text{V}_\text{O})$, (c) $\text{Fe-O}_3(\text{V}_\text{O})_2$, and (d) $\text{Fe-O}_5(\text{ferryl O})$ ensembles.

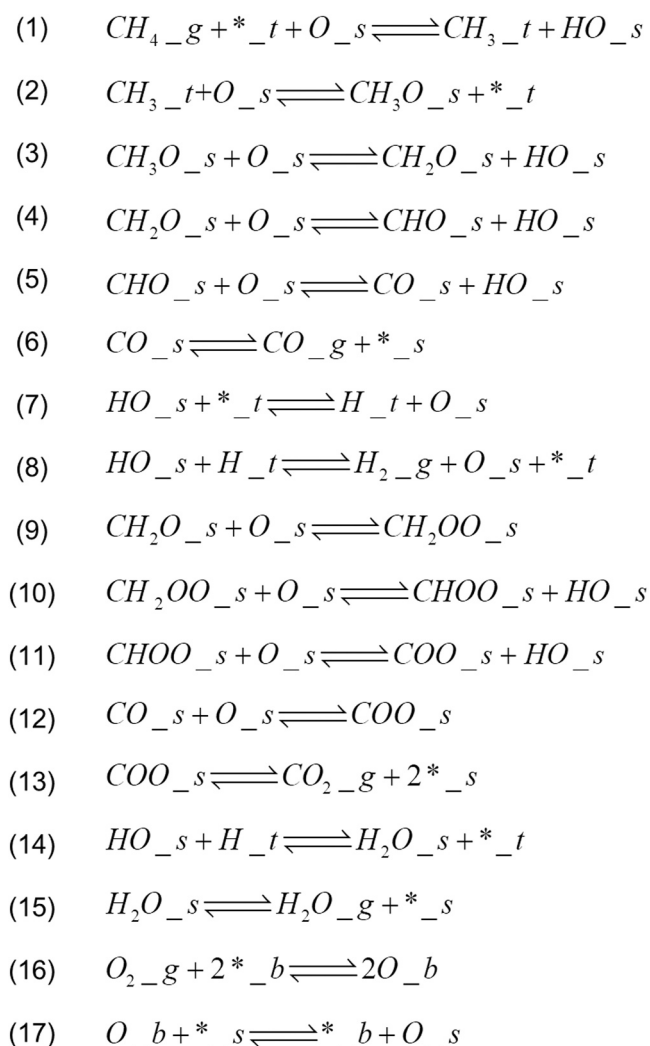
concentrations have previously been proposed by Li et al. [60], which were also constructed in this work to describe the local structures around Fe and to elucidate how the activity of the LaFeO₃ perovskites may be affected by the coordination environment of Fe (see Fig. 1b-d). The oxygen sites that may bind reaction intermediates are also illustrated in the figure. As previously proposed [66], the exposed O ions in the Fe-O₅ ensemble can be divided into two groups: O_I and O_{II}, which lie above and below the Fe cation, respectively. Comparison of the surface oxygen vacancy formation energies indicates that the O_I ion can be removed more readily than O_{II} (Table S3). As a result, the Fe-O₄(V_O) ensemble with an O_I atom removed was under consideration. Because the remaining exposed oxygen ions have different chemical identities, there are five adsorption sites existing in the Fe-O₄(V_O) ensemble: O_I, O_{II}, O_{III}, Fe, and V_O (oxygen vacancy).

After the other O_I atom participates in the redox reaction and is removed from Fe-O₄(V_O), the Fe-O₃(V_O)₂ ensemble with two neighboring oxygen vacancies results. Besides, given the fact that the fully oxidized LaFeO₃ perovskites were found to be selective toward CO₂ production at the beginning of the reaction, it is advantageous to study the methane oxidation pathways on the O-rich surface. The calculated surface phase diagrams of La-based perovskites predicted that the most stable surface termination of LaFeO₃ in the O-rich limit under mild conditions is of FeO₂ type [60]. Thus, although the ferryl oxygen that is coordinated solely to Fe (see Fig. 1d) would be present on the fully oxidized LaFeO₃ upon oxidation/re-oxidation, this type of oxygen is thermodynamically unstable and can be readily removed after reacting with methane. Furthermore, we have considered the possibility of oxygen adsorption at other sites on the stoichiometric LaFeO₃ and found that O cannot be stabilized at either the Fe or the O site because of their saturated coordination environments. We therefore took the ferryl oxygen as adsorbed surface oxygen and constructed the Fe-O₅ ensemble with a ferryl O adsorbed at the Fe site, which are denoted as Fe-O₅(ferryl O).

The local structures on LaFeO₃ measured by EXAFS have been well documented in the literature [67,68]. The measured bond lengths of Fe-O, Fe-La, and Fe-Fe in LaFeO₃ are 1.99, 3.4, and 4 Å, respectively. By comparison, the bond lengths predicted by our DFT calculations are 1.960, 3.349, and 3.881 Å on the FeO₅-terminated surface while those on the FeO₄-terminated surface are 2.035, 3.495, and 3.877 Å, which are in good agreement with the experimental values. In addition, the EXAFS studies revealed that the Fe-O bond length increases with increasing the oxygen deficiency (δ in LaFeO_{3-δ}), which is also verified by the DFT calculations. Therefore, the structural models of the LaFeO₃ surface built in the present work fit the one determined experimentally well.

2.5. Microkinetic analysis

The kinetic model for methane oxidation, including both partial oxidation and total combustion occurring at the Fe-O₅ and Fe-O₄(V_O) ensembles, is built under different reaction conditions (873–1273 K, 0.63–6.31 bar), which was solved using a modified CatMAP code [69,70] under the steady-state approximation and within the framework of the mean-field theory. The postulated reaction network for methane oxidation is illustrated in Scheme 1, where “t”, “s”, “b” and “g” represent the Fe site, the surface oxygen site, the bulk oxygen site, and the gas-phase species, respectively. Considering the minor difference in the calculated oxygen vacancy formation energies at the different oxygen sites in either the Fe-O₅ or Fe-O₄(V_O) ensemble, it is assumed to a first approximation that the O ions exposed in each the ensemble exhibit the same adsorption properties and there is no carbon deposited at the steady state. As a consequence, the ratio of O to Fe on the oxide surfaces remains constant, which equals 2 and 1.5 at a Fe-O₅ and a Fe-O₄(V_O) ensemble, respectively. To mimic the site competition of the CO and CO₂ production pathways, the reaction intermediates along the total combustion pathway are defined to occupy double oxygen sites, such as CH₂OO_s, CHOO_s, and COO_s, while along the partial oxidation



Scheme 1. Postulated Reaction Network for Methane Oxidation (t, s, b, and g represent the Fe site, the surface oxygen site, the bulk oxygen site, and the gas-phase species, respectively).

pathway the CH_x species are accommodated by only one oxygen site.

In addition, in the fuel reactor that is focused on in this work, methane is oxidized by the adsorbed or lattice oxygen of perovskites in the absence of gas-phase O₂. Nevertheless, to conduct the microkinetic analysis under the steady-state approximation and keep the mass balance, we added a “dummy” elementary step $O_{2_g} + 2*_b \rightleftharpoons 2O_b$ which is barrierless in the forward direction into the reaction network, on the assumption that this step is sufficiently fast and does not affect the kinetics of the overall reaction. It is important to note that both the bulk and surface structure is actually fully dynamic during the chemical looping process and a complete microkinetic model for the overall chemical looping process is still challenging. For this reason, here we limited our microkinetic modeling at the Fe-O₅ and Fe-O₄(V_O) ensembles, in order to elucidate the dependence of the catalytic performance of the perovskite upon the amount of oxygen vacancies on the catalyst surface.

3. Results and discussion

3.1. Catalytic performance of LaFeO₃

3.1.1. Determination of reaction conditions

Oxygen carriers or redox catalysts for chemical looping partial

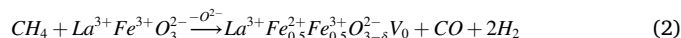
oxidation can be optimized by tailoring both the bulk and surface properties of the perovskite oxides, and the surface of the catalyst plays a critical role in the selectivity and activity [71].

Here methane oxidation was first carried out at 1093, 1133, and 1173 K to determine the influence of temperature on the deactivation of the catalyst. The flow rate of methane was 7.2 mL/min in 33 mL/min Ar. Experiments were conducted on LaFeO₃, and the reaction time was kept to 4 min to inhibit carbon formation. Even though the experiments were performed within 4 min, a small amount of carbon was produced at 1093 K. When the temperature was increased to 1133 and 1173 K, no carbon deposition was observed. The total conversion of methane and CO selectivity are shown in Fig. 2a. The CO selectivity was calculated as the ratio of the mole fraction of CO to the total mole fractions of CO and CO₂. Interestingly, it can be seen that the CO selectivity of almost 100% can be achieved at 1173 K when the reaction time is carefully controlled and methane conversion increases with temperature, which implies that the LaFeO₃ dramatically promotes methane oxidation at high operating temperatures. In light of this fact, the reaction is carried out at 1173 K in the subsequent experimental and theoretical studies.

3.1.2. Effect of oxygen vacancy on the catalytic performance of LaFeO₃

For the partial oxidation of methane, a cyclic process is proposed, where the perovskites are oxidized with a mixture of 10 mL/min O₂ in Ar and thereafter reduced with a mixture of 7.2 mL/min CH₄ in Ar for 6 min at 1173 K. In between the oxidation and reduction, the reactor was flushed with Ar to avoid mixing of gaseous methane and oxygen. These experiments were performed using LaFeO₃ as the catalyst. On the fully oxidized LaFeO₃, the total combustion leading to CO₂ and H₂O formation occurs at the beginning of the reaction [denoted as STAGE(I) in Fig. 2b], with the CO selectivity of 23%. On the basis of the transient experiment results of the CO and CO₂ formation rates as a function of time, the accumulative amount of oxygen removed from the LaFeO₃ lattice was estimated. It is well known that in the ABO₃ perovskite structure, the A site is not reducible while the B site is reducible [16,28,31]. Removal of lattice oxygen from the ABO₃ perovskite structure causes a reduction of the B site. The reduction of Fe³⁺ to Fe²⁺ was observed by an XRD study of reduced LaFeO₃ [16], and even reduction

to Fe⁰ was observed for deeply reduced LaFeO₃ [38]. XPS [30] and X-ray absorption spectroscopy [67] revealed the Fe³⁺ is dominant in LaFeO₃. The formation of Fe²⁺ and lower Fe oxidation state is related to the reduction of the perovskite structure or the formation of oxygen vacancy. Increased Fe²⁺ formation was also observed by a partial substitution of Sr for La [30]. The reduction of LaFeO₃ by methane can be described by



where δ is the oxygen deficiency that indicates the amount of removed oxygen from perovskite and V₀ represents oxygen vacancy [38]. Since the consumed oxygen would lead to the formation of oxygen vacancies, the variation of the oxygen deficiency in LaFeO₃ was then calculated based on the amount of lattice oxygen converted with time (see Fig. S1a), which is correlated with the rates of formation of CO and CO₂ on LaFeO₃ in Fig. S1b and S1c.

After STAGE(I) and during the major part of the reaction [denoted as STAGE(II) in Fig. 2b], the methane total oxidation shifts to selective partial oxidation to CO and H₂, where the CO selectivity of 98% is attained. When the reduction time approaches 4.5 min which corresponds to an oxygen deficiency of 0.30, an increase in the H₂/CO ratio was observed, indicating that carbon deposition begins to take place at the catalyst deactivation stage [which is denoted as STAGE(III) in Fig. 2b]. Meanwhile, the CO selectivity of 96% was observed, suggesting that CO₂ was suppressed at this stage. The measured H₂/CO ratio as a function of reduction time over the fully oxidized LaFeO₃ at 1173 K is shown in Fig. S2.

The re-oxidation of the reduced LaFeO_{3- δ} is shown in Fig. 2d and e. The oxygen achieves full conversion up to the breakthrough time of about 3.5 min (see Fig. 2d), and the oxidation rate is much faster than the reduction rate. CO and CO₂ were detected in the re-oxidation process, suggesting carbon is formed during the reduction. As aforementioned, carbon can be formed during the reduction step at STAGE(III), especially on the perovskites with higher oxygen vacancies [16].

The fully re-oxidized LaFeO₃ shows a similar catalytic performance to that of the fresh catalysts, where CO₂ formation dominates at the

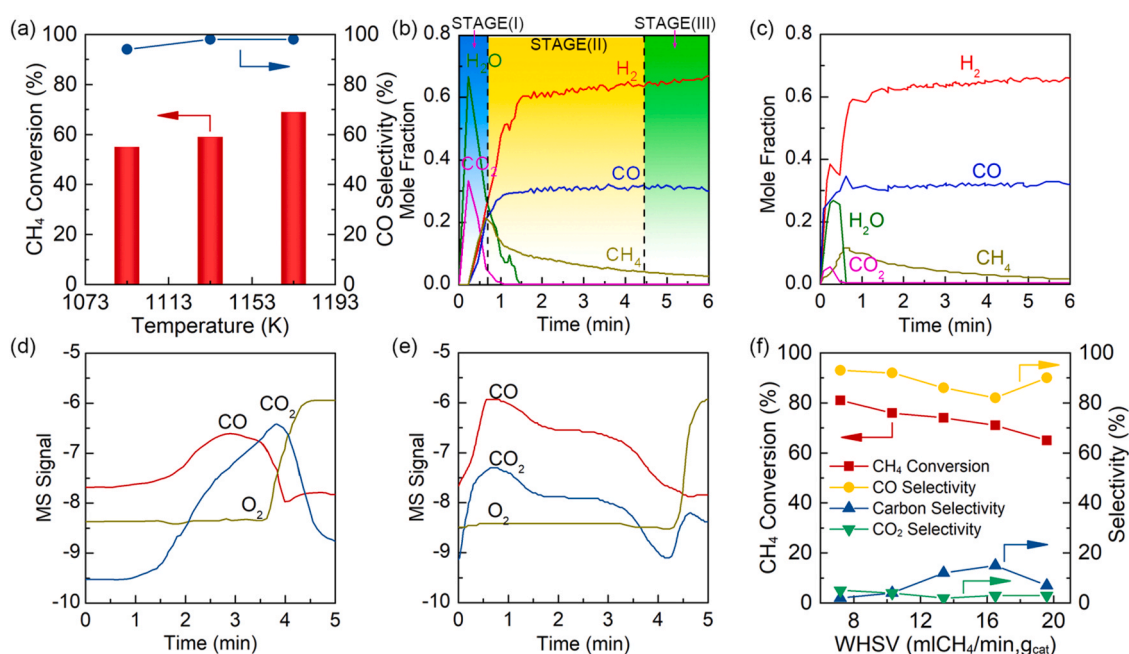


Fig. 2. (a) The CH₄ conversion and CO selectivity during methane oxidation as a function of temperature; results from reaction of CH₄ at 1173 K represented as the mole fractions of the gases as a function of reduction time over (b) fully and (c) partially oxidized LaFeO₃; MS signals from (d) re-oxidation of LaFeO₃ after five cyclic experiments and (e) re-oxidizing LaFeO₃ after conducting an experiment with 16 mL/min_{g_{cat}} CH₄ in Ar for 6 min at 1173 K; (f) the CH₄ conversion and catalyst selectivity as a function of WHSV.

initial stage.

Fig. S1 suggests that total combustion occurs at high oxygen contents at the initial stage or low amounts of oxygen vacancies (The amount of removed O changes from 0 to 0.25 mmol/g_{cat}). There is an oxygen deficiency threshold of 0.08 in LaFeO_{3-δ}, beyond which fully selective methane partial oxidation to synthesis gas is achieved. One may argue that at the initial stage the total combustion results solely from the enrichment of the surface electrophilic O₂⁻ or O⁻ species. To identify the critical factor determining the selectivity, a comparative experiment was carried out, where a similar oxygen deficiency is attained by carefully controlling the injection of the proper amount of oxygen through the re-oxidation of the reduced catalyst.

It is found that six minutes of reduction removes 1.64 mmol/g_{cat} oxygen and generates an oxygen deficiency of 0.40 in LaFeO_{3-δ}. The re-oxidation time was then varied and optimized to be 95 s and an oxygen deficiency of 0.10 results, which is slightly larger than the oxygen vacancy concentration threshold. On the LaFeO_{2.9}, almost fully selective partial oxidation of methane to CO and H₂ has been achieved (see Fig. 2c) and CO₂ formation is completely suppressed, indicating that surface electrophilic O₂⁻ or O⁻ species cannot be generated at such an oxygen deficiency. Moreover, because the deficiency of 0.1 implies more than the ferryl oxygen is removed from the oxide, there must be some oxygen vacancies (The ferryl oxygen is taken as the adsorbed oxygen rather than lattice oxygen) present on the LaFeO_{2.9} surface, which make the material selective toward syngas. These findings reveal that the oxygen deficiency is a critical parameter in controlling the selectivity. Based on the result, a new strategy of controlling the re-oxidation time is proposed to control the oxygen deficiency to be larger than the threshold and hence to achieve fully selective partial oxidation of methane. More interestingly, it is possible for the LaFeO₃ perovskite to produce synthesis gas with a H₂/CO ratio close to 2 (the stoichiometric ratio) with high conversion and CO (and H₂) selectivity. The conversion is around 90% and the CO selectivity is almost 100%, so the partially oxidized LaFeO_{3-δ} shows a great promise as a catalyst candidate for the partial oxidation of methane.

To further validate the strategy, the method of controlling the oxygen deficiency was explored on the La_{0.8}Sr_{0.2}FeO_{3-δ} catalyst as well. The product distribution of methane oxidation on La_{0.8}Sr_{0.2}FeO₃ by oxidation/reduction cycles at 1173 K is shown in Fig. S3a. The oxygen deficiency threshold for selective methane oxidation on La_{0.8}Sr_{0.2}FeO_{3-δ} was found to be 0.10 in Fig. S4. It is higher than that in LaFeO_{3-δ} (δ = 0.08), which is most likely due to the higher oxygen mobility of lattice oxygen in La_{0.8}Sr_{0.2}FeO_{3-δ} than in LaFeO₃ [30]. Six-minute reduction by methane removes 1.36 mmol/g_{cat} and generates an oxygen deficiency of 0.32 in La_{0.8}Sr_{0.2}FeO_{3-δ}. The re-oxidation time was then varied and optimized to be 85 s to precisely control the amount of oxygen injected to the perovskite to achieve fully selective conversion to synthesis gas. By taking the average oxidation rate of the La_{0.8}Sr_{0.2}FeO_{3-δ} by subtracting the carbon oxidation, 85 s of re-oxidation results in the oxygen deficiency of 0.21, larger than the corresponding threshold. Again fully selective methane oxidation was also attained (Fig. S3b); that is, we can achieve fully selective methane partial oxidation on both LaFeO_{3-δ} and La_{0.8}Sr_{0.2}FeO_{3-δ} by controlling the degree to which the perovskites are oxidized, independent of the catalyst material.

Moreover, we have examined the effect of the oxygen deficiency on the structural stability of Lanthanum-based perovskites in a previous study [72]. A sharp increase in the oxygen vacancy formation energy was observed when the oxygen deficiency is increased to 0.50, which means that there exists a maximum possible oxygen deficiency of 0.50 at which non-stoichiometric LaFeO_{3-δ} may possibly maintain a stable crystal structure and beyond which the ternary oxide may collapse into mixed binary oxides. In our experiments, the perovskites are oxidized with a mixture of 10 mL/min O₂ in Ar and thereafter reduced with a mixture of 7.2 mL/min CH₄ in Ar for 6 min at 1173 K. Upon reduction the oxygen deficiency is about 0.40 in LaFeO_{3-δ}, so the perovskite crystal structure can be maintained.

In summary, the oxygen deficiency (i.e., the oxygen vacancy concentration) or lattice O concentration in perovskites is a critical parameter in determining the selectivity in methane oxidation. There is an oxygen deficiency threshold in La-based perovskites for the selective methane partial oxidation. In other words, apart from substitution for the A- or B-site cations in the La-based perovskites [30], altering the oxygen deficiency larger than the threshold by controlling the degree of oxidation of perovskites is a promising strategy for improving the catalyst selectivity and achieving fully selective methane partial oxidation.

3.1.3. Effect of WHSV on the catalytic performance

To investigate the effect of WHSV on the oxidation performance, experiments were performed, where the flow of methane was increased during the repeated reduction/oxidation cycles (Table S4). Oxidation of methane on the LaFeO₃ was performed using 5 different flows of methane. All experiments were performed at 1173 K with a total flow of 40 mL/min, reaction time of 6 min of methane, and 1 g catalyst. After all the experiments, the perovskites are fully re-oxidized to their equilibrium oxygen content by O₂/Ar.

As can be seen in Fig. 2f, the conversion of methane drops with the increase in WHSV as expected. Furthermore, based on the MS data, the amount of carbon formed during the reduction period was estimated and the selectivity toward carbon formation is also presented. As reflected in the shift in the CO and CO₂ peak to the short time (see Fig. 2d and e), the selectivity toward carbon increases and the carbon becomes difficult to remove with increasing the space velocity. Meanwhile, the CO and CO₂ selectivity remain more or less constant while varying WHSV (see Fig. 2f), indicating that CO₂ is not produced by CO oxidation but rather is a primary product of methane oxidation. Hence, the dramatic change in the catalyst selectivity as observed at STAGE(I) and STAGE(II) of the reaction must be accompanied by the dynamic transition of the active sites on the catalyst surface. A full picture of how the catalytic performance would be determined by the nature of the active sites can only be achieved through an understanding of the step-by-step molecular pathways leading from reactants to products.

3.2. Adsorption properties of LaFeO₃

According to the Brønsted-Evans-Polanyi (BEP) relationship [73,74], the activity of methane dissociation is determined largely by the adsorption behaviors of CH_x and H on the surface. Fig. 3a presents the calculated H adsorption energy (ΔE_{ads,H}) at the four active ensembles. A negative value shows the exothermic nature of H adsorption (see Table S5), and the more negative the value, the more strongly does H interact with the surface. It can be seen from the figure that H is bound more tightly to O. To interpret the reactivity of the O ions on the terminations in terms of their electronic structures, the local density of states (LDOS) projected onto the O 2p orbitals are then calculated, as illustrated in Fig. 3b-e. One can see that at the Fe-O₅ ensemble (see Fig. 3b) the energy of the O_{II} 2p orbital is shifted to a more negative value than that of O_I and, consequently, the O_{II} ion has less unoccupied states near the Fermi level; that is, the O_{II} ion carries more electrons and shows a diminished ability to gain electrons. As the atomic H bonded to the O site donates electrons to the oxygen ions and carries positive charges, O_I binds H more strongly than O_{II}. The same reason suggests the ferryl O and O_I ions are more capable of adsorbing H at the Fe-O₅(ferryl O) and Fe-O₄(V_O) ensembles, respectively. Comparison of the adsorption energies of H at the different ensembles shows that H interacts less strongly with O at the ensembles having more oxygen vacancies, which is due to the fact that the electrons left behind upon removal of an oxygen atom would delocalize over the whole surface and the increased electron density on the remaining O ions would limit their ability to adsorb H [66].

The optimized geometries of the carbon-containing reactants, products, and intermediates adsorbed on LaFeO₃ are presented in Fig. S5 and

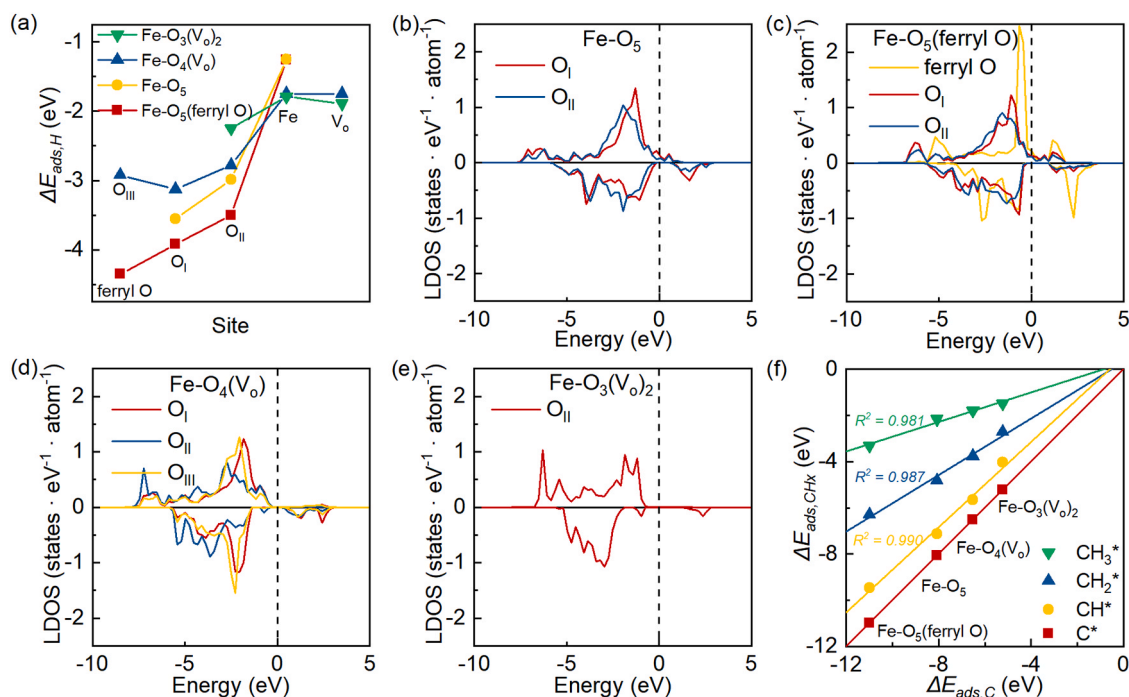


Fig. 3. (a) Comparison of adsorption energies of atomic hydrogen at different sites in the four Fe coordination environments, as well as the LDOS projected onto oxygen ions in the (b) Fe-O₅, (c) Fe-O₅(ferryl O), (d) Fe-O₄(V_o), and (e) Fe-O₃(V_o)₂ coordination environments; (f) scaling relations between adsorption energies of CH_x (x = 0–3) and atomic C in the four Fe coordination environments.

the calculated adsorption energies are summarized in Table S6 where only the lowest-energy configurations are taken for the subsequent analysis. The CH₄ interacts weakly with the different ensembles and the distance between the C atom and surface is greater than 3 Å. The adsorption energy of CH₄ is about −0.20 eV, which falls within the typical range resulting from London dispersion forces. Except for the CH₃ and CH₂ fragments that are accommodated by the Fe and V_o site in the Fe-O₃(V_o)₂ ensemble, respectively, all the CH_x (x = 0–3) species are preferentially coordinated to the active oxygen ions, in accord with the predictions by the aforementioned DOS analysis that the ferryl O, O_I, O_{II}, and O_{III} sites play a major role in the adsorbate-substrate interaction at the Fe-O₅(ferryl O), Fe-O₅, Fe-O₄(V_o), and Fe-O₃(V_o)₂ ensemble, respectively.

At the Fe-O₅(ferryl O) ensemble having three types of exposed oxygen ions, CH_x is found to be preferentially bound to the ferryl O because it has even less electrons than the O_I ion. Even if C is initially positioned at the O_I-O_I site, the bond between the ferryl O and the underlying Fe cation would be cleaved, and the ferryl O would be bonded to the carbon atom via a third C-O bond, achieving the most stable structure. At the first three ensembles, CH₂ and CH are bonded to two O ions so that the lattice O ions are taken upward and positioned far away from the oxide surface, leading to the formation of CH₂OO and CHOO. As for C, it would be relaxed to the adjacent active O ion upon geometry optimization even though initially positioned at the Fe site, resulting from its unsaturated coordination environment. In particular, the most stable adsorption configuration results at the Fe-O₅ ensemble when C is bonded to three oxygen ions (two O_I ions and an O_{II} ion). At the Fe-O₄(V_o) ensemble, although the CH and C are thermodynamically preferred by the Fe-O_{II} site, all the CH_x species can be stabilized at the V_o site by bridging two Fe ions, which is due primarily to the fact that the increase in the electron density on the remaining Fe cations upon removal of oxygen atoms facilitates the electron transfer from Fe to the CH_x.

Fig. 3f depicts the calculated adsorption energies of CH_x (0–3) as a function of the adsorption energy of atomic carbon at the different ensembles. As indicated in this figure, the adsorption energies of the reaction intermediates become more negative on going from CH₃ to C at

each active ensemble. In particular, the strong bonding between atomic C and lattice O makes it favorable for CO or CO₂ to be released from the oxide surface by the Mars van Krevelen mechanism. Further comparison of the adsorption energies of the same adsorbate at the different ensembles reveals that the adsorption strength of the intermediates increases from Fe-O₃(V_o)₂ through Fe-O₄(V_o) and Fe-O₅ and eventually to the Fe-O₅(ferryl O) ensemble; that is, the CH_x species interact more weakly with O at the ensembles having more oxygen vacancies, following the same trend as that observed for the bonding between H and O. Interestingly, the adsorption energies of CH_x scale linearly with that of atomic C, suggesting that the chemisorption energy scaling relations reported on metals and perovskites [63,75–77] hold well even if the composition of the oxide is not varied.

3.3. Methane oxidation on LaFeO₃

According to the many elementary steps involved in Scheme 1, methane oxidation proceeds by way of two parallel reactions: partial oxidation and total combustion. Besides, carbon deposition may take place. Armed with the knowledge of the adsorption behaviors of the reaction intermediates on LaFeO₃, we are now in a position to explore how CH₄ would be activated to form CO, CO₂, and carbon and to reveal the nature of the active sites. It is known that the C-H bond can be activated by the Fe-O/O-O and Fe-Fe sites on the surface [78,79]. Cheng et al. proposed that methane would be dissociated heterolytically on Fe₂O₃(001), giving rise to CH₃-Fe and H-O [42]. Given the long distance between the two Fe cations on the surface of the perovskite, only the Fe-O and O-O sites are taken into consideration in this work to investigate the C-H bond activation, aiming at identifying the ensemble requirements of the partial oxidation and total combustion of methane.

3.3.1. Total combustion of CH₄ at the Fe-O₅(ferryl O) ensemble

After LaFeO₃ is fully oxidized, the ferryl O is most likely to be exposed on the perovskite surface, which therefore accounts for the fast total combustion occurring at the beginning of the reaction. Since the ferryl O interacts strongly with the adsorbates, it is reasonable to expect

that the ferryl O species are highly active and capable of activating C-H bonds. It is found that CH_4 is dissociated at the ferryl O site by a radical mechanism (see TS1 in Fig. 4), in much the same way as that observed in the oxidative coupling of methane [80]. The energy barrier for the activation of the first C-H bond is calculated to be 0.60 eV and we will see that this barrier is lowest among the activation energies at the different active ensembles having different Fe coordination environments (see Table S7). The H atoms that are abstracted from the methane could also be accommodated by the O_I and O_{II} ions. Basically, the adsorption of the generated H on the oxide surface would not only reduce the active sites of the reaction but also have a significant impact on the neighboring active sites. Li et al. [66] studied the H migration process on FeO_2 , and found that long-range hydrogen transport on the oxide surfaces follows a “vehicle” mechanism in which hydrogen hops together with the underlying oxygen and the hopping is quite facile. Thus, before the further dehydrogenation step, the active O sites would return to their original state or become oxygen-deficient after H_2 or H_2O is released. It turns out that the ferryl $\text{O}-\text{O}_I$ site is involved in the formation of H_2O (see TS5' in Fig. 4) while the $\text{Fe}-\text{O}_I$ site serves as the active site for H_2 desorption (see TS5 in Fig. 4). Comparison of the energy barriers suggests that H_2O formation is both kinetically and thermodynamically more favorable, as illustrated in Fig. S6.

Upon dissociation of CH_4 , CH_3 is adsorbed favorably at the ferryl O site, leading to the formation of CH_3O . Then, the second dehydrogenation step would occur at the ferryl O and O_I ion pair, and the radical mechanism no longer prevails. When the CH_3O fragment is activated, the carbon-containing species would form a σ bond to the neighboring O_I ion, giving rise to CH_2OO . In each of the subsequent dehydrogenation steps, a third oxygen ion participates in the reaction by attacking one C-H bond, and CO_2 would be finally desorbed from the surface with a low energy barrier of approximately 0.10 eV, leaving the local structure with two oxygen vacancies. Thus, at the beginning of the reaction, three

oxygen ions bring about the total combustion of methane at the $\text{Fe}-\text{O}_5$ (ferryl O) ensemble, and CO_2 may result without the formation of CO ; that is, CO_2 is a primary product of methane oxidation rather than a secondary product of CO oxidation.

The Gibbs free energy diagram for the total combustion and partial oxidation at the $\text{Fe}-\text{O}_5$ (ferryl O) ensemble is illustrated in Fig. 4. Because in such a diagram the point with the highest energy usually defines the slowest step, it follows that the first dehydrogenation step controls the rate of the overall reaction in both the two cases. Furthermore, comparison of Gibbs free energy diagrams between total combustion and partial oxidation of methane (see Fig. 4) also demonstrates that methane tends to be fully combusted at the $\text{Fe}-\text{O}_5$ (ferryl O) ensemble with a high oxygen concentration, which further indicates that the total combustion of methane occurs on the fully oxidized catalyst, and the limited ferryl O ions are believed to act in such a way that CO_2 is not the secondary product of CO oxidation.

3.3.2. Total combustion of CH_4 at the $\text{Fe}-\text{O}_5$ ensemble

After the ferryl O ions are consumed via methane total combustion, two O_I and two O_{II} oxygen ions are exposed surrounding each Fe in the outermost layer and active for methane oxidation. The Gibbs free energy diagram for methane oxidation at the $\text{Fe}-\text{O}_5$ ensemble (see Fig. 5a), together with the geometries of the transition states for the elementary steps involved, are shown in Fig. 5, where the lengths of the activated C-H bonds are also given. Comparison of calculated activation energies for the first dehydrogenation step shows that the energy barrier is much lower at the Fe and O ion pair than at the O site (see Table S7), meaning that the C-H bond is likely to be activated by the heterolytic mechanism rather than by the radical mechanism. The energy barrier is calculated to be 1.17 eV at the $\text{Fe}-\text{O}_I$ site and the activated C-H bond is elongated to 1.441 Å. In the transition state, the CH_3 fragment is bound to the Fe site while the detached H is bonded to the O ion. This geometry closely

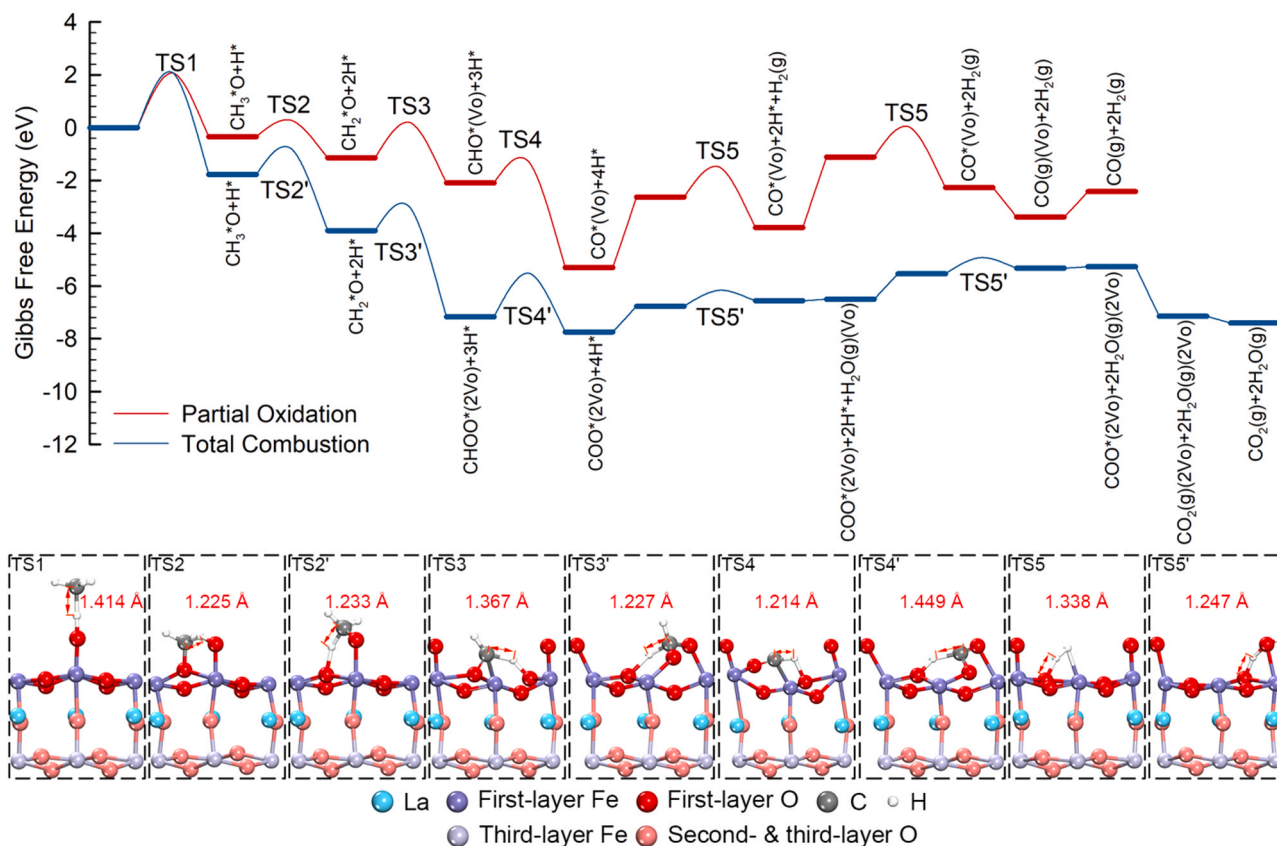


Fig. 4. Gibbs free energy diagrams for total combustion and partial oxidation of methane at the $\text{Fe}-\text{O}_5$ (ferryl O) ensemble as well as the geometries of the transition states for the elementary steps involved. All the Gibbs free energies are referenced to the sum of the Gibbs free energies of the clean surface and CH_4 in the gas phase.

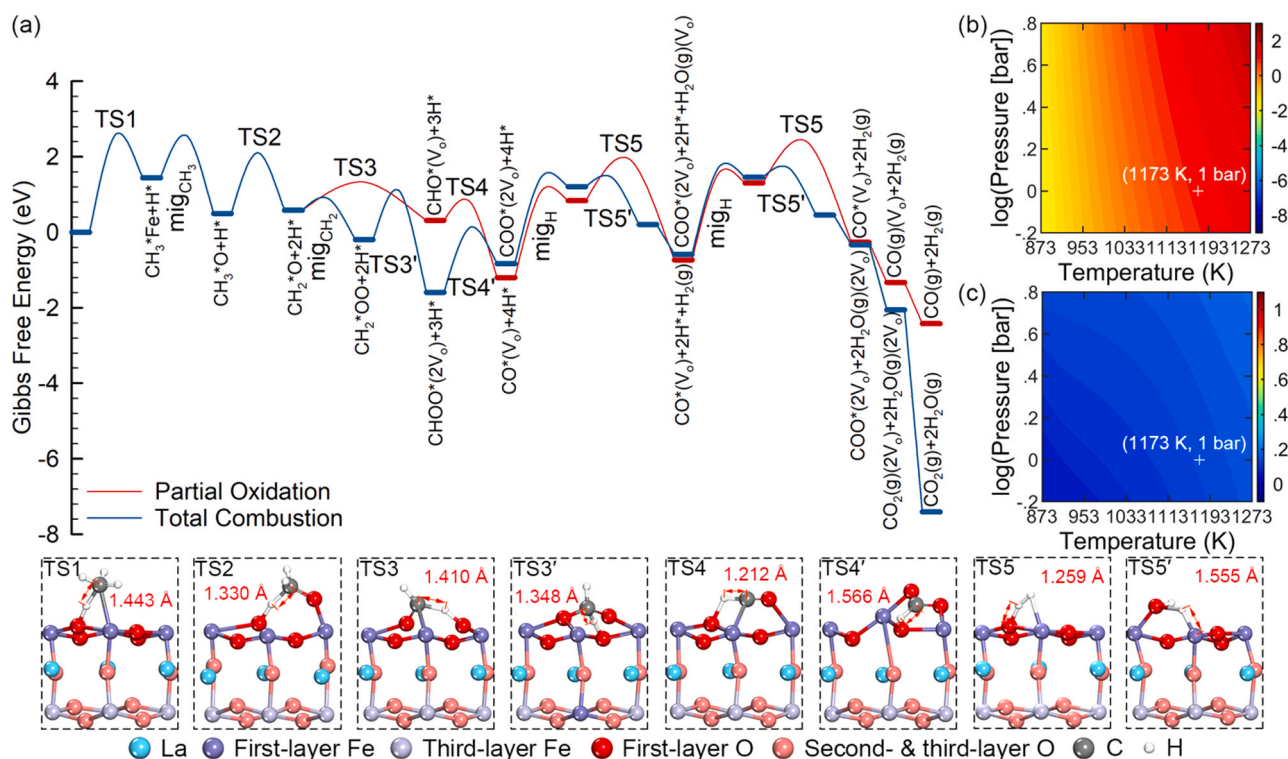


Fig. 5. (a) Gibbs free energy diagrams for the total combustion and partial oxidation of methane at the Fe-O₅ ensemble as well as the geometries of the transition states for the elementary steps involved; plots of (b) TOF for CH₄ consumption and (c) CO selectivity as functions of temperature and pressure. All the Gibbs free energies are referenced to the sum of the Gibbs free energies of the clean surface and CH₄ in the gas phase.

resembles that of the activated complexes for CH₄ dissociation on Co₃O₄(110) [81,82]. The resultant CH₃ could be dehydrogenated at the Fe-O₁ site and H is coordinated solely to the O ion in the final state. Alternatively, since CH₃ is preferentially bound to lattice oxygen to form CH₃O, it could migrate from the Fe ion to the O₁ ion with a low energy barrier of 0.72 eV and then be decomposed at the O₁-O₁ site. Comparison between the energy barriers for CH₃ dissociation at the Fe-O₁ and O₁-O₁ sites reveals that the CH₃ activation at the O₁-O₁ site is both kinetically and thermodynamically favorable, as shown in Fig. S7. Thus, only the Gibbs free energy diagram at the O₁-O₁ site is given in Fig. 5. Upon dissociation of CH₃, the resulting CH₂ would be bound to the O₁ ion and form an extra bond to the adjacent Fe cation due to its unsaturated coordination environment. Therefore, the CH₂ adsorbed at the Fe-O₁ site is taken into consideration for the subsequent dehydrogenation step along the methane partial oxidation pathway. Interestingly, when the adsorbate is bonded to the Fe-O₁ site, the lattice oxygen is likely to be taken out of the surface. As a consequence, a second oxygen ion participates in the reaction by attacking one of the C-H bonds, and CHO is formed above an oxygen vacancy and is further dehydrogenated to yield CO. Thus, methane partial oxidation could occur at the Fe-O₅ ensemble.

The CH₂ generated could also migrate from the Fe-O₁ site to the O₁-O₁ site, with a low energy barrier of 0.35 eV. We will see later that this step bears direct relation to the formation of CO₂. Then, one of the C-H bonds in CH₂ is attacked by a third oxygen ion (O₁₁), as shown in TS3' of Fig. 5, with the energy barrier calculated to be 1.58 eV. The last C-H bond is cleaved in much the same way as that in the CH₂ dehydrogenation, and CO₂ would be readily formed by surmounting an energy barrier of less than 0.10 eV, leaving the local structure with two oxygen vacancies. Thus, three oxygen ions are involved in the total combustion of methane at the Fe-O₅ ensemble, indicating that on the oxide surface where there is a high degree of site heterogeneity CO and CO₂ formation have different ensemble requirements. Moreover, comparison of the energy barriers for CO desorption and CO oxidation given in Table S8 demonstrates again that CO₂ is a primary product of methane oxidation rather

than a secondary product of CO oxidation. Either CO or CO₂ may result when specific ensemble requirement is fulfilled. Apparently, CO₂ formation is favored by a higher surface oxygen concentration.

Comparison of the Gibbs free energy diagrams for the partial oxidation and total combustion of methane at the Fe-O₅ ensemble indicates that the first dehydrogenation step is rate-determining and the adsorption strength increases from Fe through Fe-O and eventually to the O-O site, implying that the production of CO₂ is thermodynamically more favorable. However, the energy barriers for the elementary steps involved in partial oxidation are much lower than those for the total combustion. Hence, it seems quite difficult to infer simply from the discussion of the energetics of the two parallel competing reactions whether CO or CO₂ is the main oxidation product at the Fe-O₅ ensemble.

The similar question arises when discussing the evolution of hydrogen. As aforementioned, the hydrogen atoms abstracted from CH_x would first be adsorbed at the O₁ site. In an early study, Lin et al. [83] found that the H atoms prefer to be adsorbed on top of the oxygen ions on the SrTiO₃ surface at low coverages. As the hydrogen coverage increases, the H atoms begin to be adsorbed at the metal sites adjacent to the O ions. Because the Fe-O site is essential to hydrogen recombination, H atoms need to migrate to the Fe site before they can recombine to desorb from the surface. The coadsorbed H atoms may either recombine to form H₂ or react with the surface O ion to produce water, as illustrated in TS5 and TS5', respectively.

To gain deeper insight into the activity for CH₄ conversion and CO production in a more quantitative way, the turnover frequency (TOF) for methane consumption and the CO selectivity which is defined as TOF (CO production)/TOF(CH₄ consumption) are calculated as functions of temperature and pressure by using microkinetic analysis, as shown in Fig. 5b and c, respectively. From Fig. 5b, it can be seen that the TOF for CH₄ consumption increases dramatically with temperature but varies to a less extent with pressure, especially at low temperatures. More importantly, it can be seen from Fig. 5c that the CO selectivity is only 12% at the Fe-O₅ ensemble under the reaction conditions of interest in

this work (1173 K and 1 bar of CH_4 and O_2), indicating that the total combustion of methane would dominate the overall kinetics and the main oxidation products are CO_2 as well as H_2O . The calculated coverages of intermediates and free site as a function of pressure and temperature have been shown in Fig. S8 in the Supporting Information. From the figure, one can see that, as expected, the coverages of all the reaction intermediates other than the concentration of bulk oxygen (O_b) are negligibly small, indicating that oxygen diffusion is very likely to be one of the rate-determining steps for the overall process. These findings are in remarkably good agreement with the aforementioned experimental observations at the beginning of the reaction [STAGE(I)], implying that the local structure around Fe is likely to have a Fe-O_5 (ferryl O) or a Fe-O_5 coordination environment.

3.3.3. Partial oxidation of CH_4 at the $\text{Fe-O}_4(\text{V}_\text{o})$ ensemble

After an O_I atom is removed, three different oxygen ions (O_I , O_II , and O_III) are exposed in the $\text{Fe-O}_4(\text{V}_\text{o})$ ensemble containing an oxygen vacancy. In our used model, it gives an oxygen deficiency of 0.167 that is larger than the oxygen deficiency threshold of 0.08 observed in Section 3.1.2. The calculated results shown in Fig. S9 in the Supporting Information and the aforementioned experimental findings demonstrate that surface electrophilic O_2^- or O^- species cannot be present at such an oxygen deficiency, implying that methane partial oxidation may be dominant at the $\text{Fe-O}_4(\text{V}_\text{o})$ ensemble. The geometries of the transition states for the elementary steps involved in the methane oxidation at the $\text{Fe-O}_4(\text{V}_\text{o})$ ensemble are shown in Fig. 6a, where the lengths of the activated C-H bonds are also given. Upon physisorption CH_4 has one of the C-H bonds broken, leaving CH_3 and H bonded to the Fe cation and O_I ion, respectively. The energy barrier is calculated to be 0.89 eV at the Fe-O_I site and the activated C-H bond is elongated to 1.399 Å. It was reported that the resultant H can be transferred on the defective surface by the “vehicle” mechanism [66], and the Fe-O_I site may be restored to its original state by accepting an oxygen ion from bulk oxide. Then, in the

transition state for CH_3 dehydrogenation, CH_2 may form a σ bond to each of the two neighboring surface Fe cations and sits in the oxygen vacancy between them. Alternatively, CH_3 may first migrate to the energetically more favorable O_I site (Table S9) and then has the three C-H bonds broken successively and in the same way as that described at the Fe-O_5 ensemble. The only difference is that on the oxygen-deficient surface the O_I ion which serves as the active site for the partial oxidation and total combustion of methane becomes less reactive.

As aforementioned, the formation of H_2 and H_2O are parallel competing reactions, implying that the H_2 production would inhibit the production of H_2O . In light of this information, the comparison of the energy profiles for the formation of H_2 and H_2O at different ensembles is shown in Fig. S6, where the geometries of the transition states are also involved. It can be seen that, at the Fe-O_5 ensemble where three oxygen ions are exposed, the H-O bond is elongated to 1.448 Å and both hydrogen atoms form a σ bond to each other, leading to the formation of H_2 , while H_2O formation results from the two H atoms bonded to the same oxygen which is taken out of the surface. Moreover, a lower energy barrier for hydrogen recombination than for H_2O formation is observed at the Fe-O site on the O-deficient surface, meaning that H_2 formation is kinetically more favorable.

Furthermore, the energy barriers for the recombination of hydrogen at the Fe-O site become lower when more oxygen vacancies are present, indicating that H_2 formation occurs favorably on the O-deficient surface (see Table S10).

Comparison of the Gibbs free energy diagrams for the partial oxidation of methane, total combustion of methane, and carbon deposition in Fig. S10 reveals that at the $\text{Fe-O}_4(\text{V}_\text{o})$ ensemble the overall Gibbs free energy barrier for carbon deposition at the $\text{V}_\text{o}-\text{O}$ site is markedly higher than the other two pathways, indicating that carbon deposition can be neglected. Hence, only the Gibbs free energy diagrams for the partial oxidation and total combustion of methane are given in Fig. 6a. It can be seen that the production of CO_2 is thermodynamically

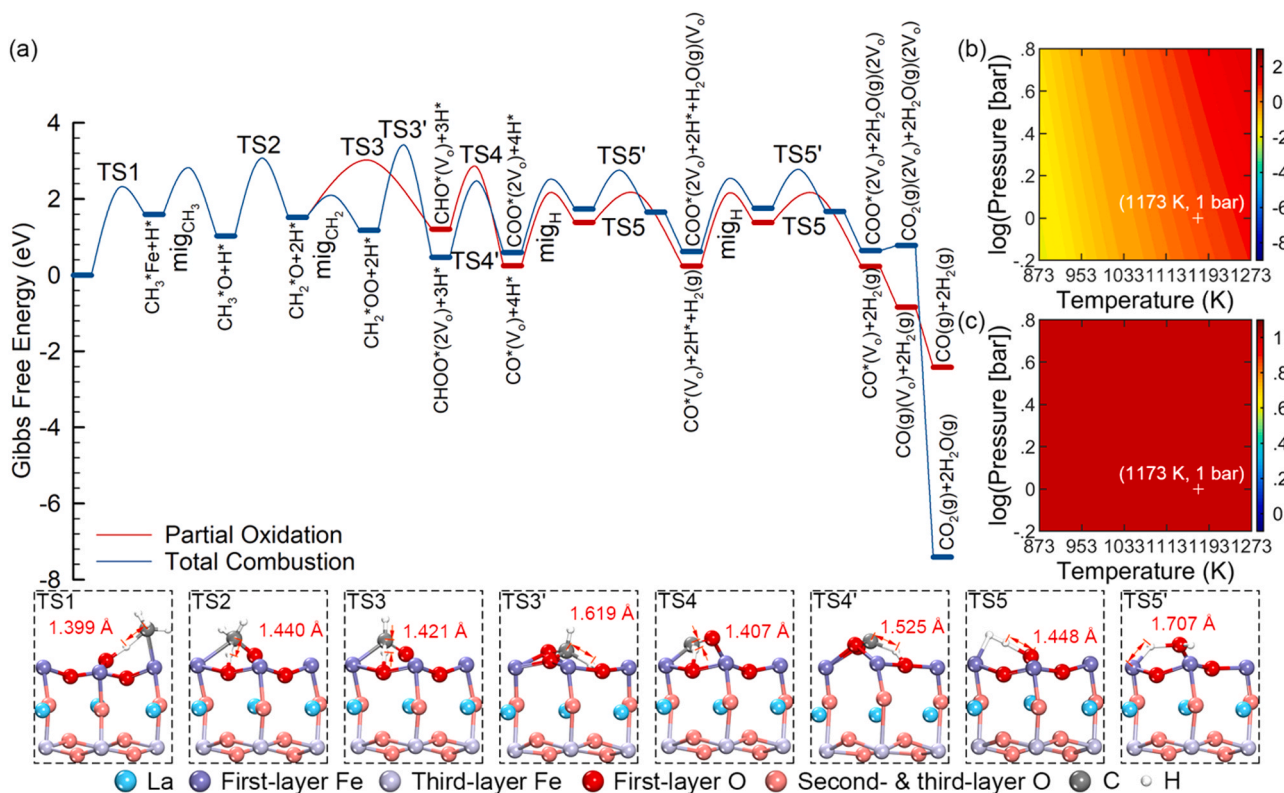


Fig. 6. (a) Gibbs free energy diagrams for the total combustion and partial oxidation of methane at the $\text{Fe-O}_4(\text{V}_\text{o})$ ensemble as well as the geometries of the transition states for the elementary steps involved; plots of (b) TOF for CH_4 consumption and (c) CO selectivity as functions of temperature and pressure. All the Gibbs free energies are referenced to the sum of the Gibbs free energies of the clean surface and CH_4 in the gas phase.

more favorable while the energy barriers for the elementary steps involved in partial oxidation are lower than those for the total combustion, the same as that observed at the Fe-O₅ ensemble. Hence, a detailed microkinetic analysis was also performed to give a reasonably accurate description of the competition between partial oxidation and total combustion of methane.

The calculated TOFs for methane consumption and CO selectivity are shown in Fig. 6b and c, respectively. Comparison of the TOFs for methane consumption at the Fe-O₅ and Fe-O₄(V_o) ensembles reveals a higher rate of CH₄ conversion at the Fe-O₅ ensemble, indicating that the rates for methane oxidation are accelerated by the higher surface oxygen concentration. More importantly, it can be seen from Fig. 6c that a very high CO selectivity of 99% is predicted, meaning that the partial oxidation of methane is predominant and a fully selective conversion to CO can be achieved at the Fe-O₄(V_o) ensemble. It is important to note that DFT has an inherent uncertainty of about 0.2 eV in the calculated activation energies and reaction heats for elementary steps. It is therefore difficult to compare the theoretically calculated TOF directly to the experimental data, but the trend in the activity across different materials or different active sites can usually be captured by using DFT-assisted microkinetic analysis. Here the CO selectivity was calculated as the rate of formation of CO divided by the rate of consumption of CH₄, which is essentially a relative quantity, and we found that the calculated CO selectivity (99%) is in fairly good agreement with the experimental data (98%). The reason for the high CO selectivity is that the presence of surface oxygen vacancies would dramatically increase the overall energy barrier for total oxidation (as can be seen in the comparison between Figs. 5a and 6a). Therefore, at STAGE(II), the catalyst surface is most likely to be oxygen-deficient and enriched in the active ensembles that have a Fe-O₄(V_o) coordination environment, which also explains why the partially oxidized LaFeO₃ perovskite gives rise to a high CO selectivity.

3.3.4. Deactivation at the Fe-O₃(V_o)₂ ensemble

At the Fe-O₃(V_o)₂ ensemble where the two O_I atoms are removed, the geometries of the transition states for the dehydrogenation steps along

the partial oxidation of methane and carbon deposition pathways are shown in Fig. 7. As can be seen in Fig. 7, the transition states for the first dehydrogenation step are quite similar in geometry at the Fe-O₅ and Fe-O₄(V_o) ensembles, where one of the C-H bonds is effectively destroyed and the detaching H atom sits at the O site, leaving the CH₃ bonded to the Fe site via a carbon-to-metal σ bond. The only difference is that the active oxygen (O_{II}) is less reactive. Then, after the second dehydrogenation step at the Fe-O_{II} site, the resultant CH₂ is most likely to be bound to the two neighboring Fe cations and sits at the vacancy site. After that, the O_{II} ion goes on to participate in the reaction by attacking the remaining C-H bonds in the transition state. In the final state for the CH dehydrogenation, one of the oxygen vacancies is occupied by a carbon atom, leading to the initial stage of catalyst deactivation observed in experiment.

Like at the Fe-O_I site, the CH₃ could migrate from Fe to O_{II}, leading to the subsequent dehydrogenation mainly occurring at the O-O site and yielding CO. For the total combustion of methane to occur, however, three surface oxygen ions should be involved in the reaction. The limited exposed oxygen involved in the Fe-O₃(V_o)₂ ensemble shows the difficulty with catalyzing CO₂ production. Hence, only the Gibbs free energy diagrams for the partial oxidation of methane and deposition of carbon are compared in Fig. 7. One can see that the highest energy of the two diagrams are rather close, indicating that both of the two competing reactions can take place and the formation of carbon would competitively inhibit the production of CO. Furthermore, it can be seen from the figure that, although the diagram for carbon deposition is quite uphill, CH₃ and CH₂ tend to be bonded to the Fe and V_o site, respectively, instead of combining with the O_{II} ion, reflecting the tendency for carbon deposition to occur. It can therefore be deduced that the deposition of carbon occurs favorably on the local structure of the perovskite surface where there is a high surface oxygen vacancy concentration or low surface oxygen content.

3.4. General discussion

In an early study [84,85], Zeng et al. showed that, depending on the

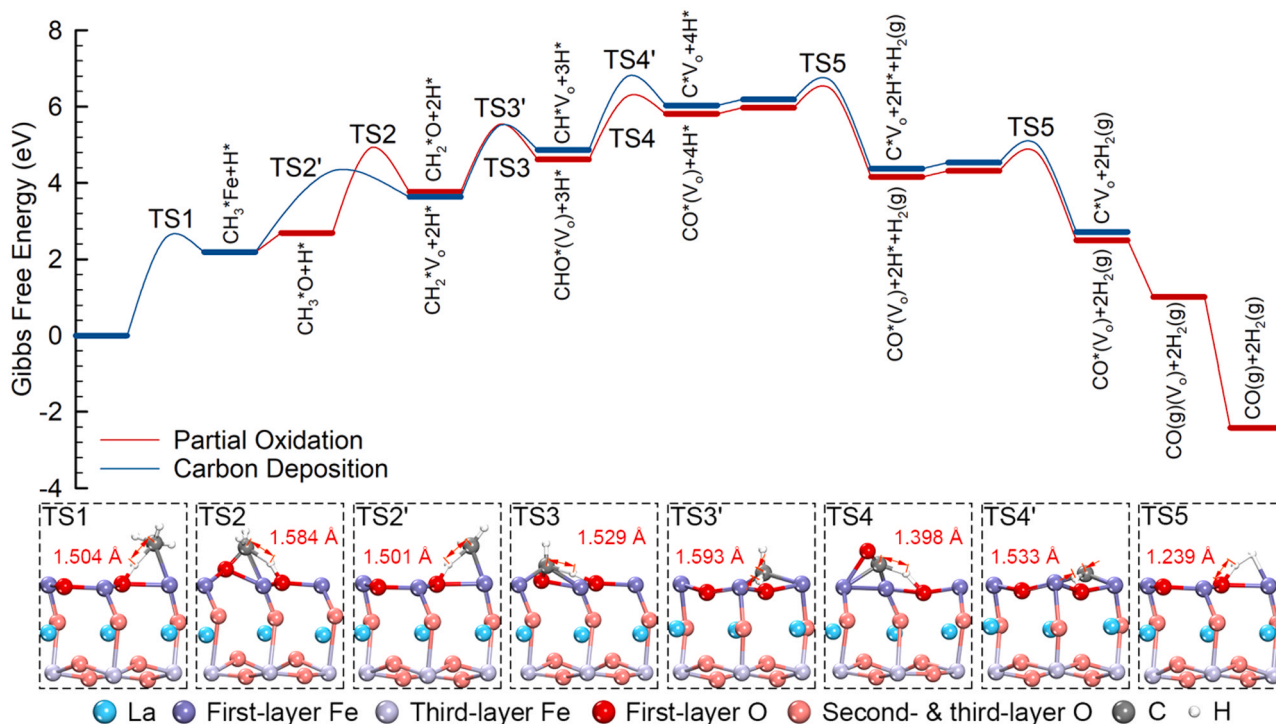


Fig. 7. Gibbs free energy diagrams for the partial oxidation of methane and carbon deposition at the Fe-O₃(V_o)₂ ensemble as well as the geometries of the transition states for the elementary steps involved. All the Gibbs free energies are referenced to the sum of the Gibbs free energies of the clean surface and CH₄ in the gas phase.

rate of oxidation reactions, the lattice oxygen either reacts directly with methane on the surface or combines to form oxygen molecules that desorb into the gas phase. Too fast oxygen release from the bulk gives a high O/CH_4 ratio on or close to the surface, favoring total combustion reactions. When the oxygen release slows down, partial oxidation becomes dominant because the effective O/CH_4 ratio is closer to 1. A too slow release of oxygen would, however, result in methane cracking and carbon formation. Meanwhile, the relation between the selectivity toward syngas and the reduction degree of the oxide was also observed by Fathi et al. [86,87], who studied the reaction between the promoted cerium oxide and methane and found that the selectivity toward syngas depends strongly on the oxidation state of the cerium oxide. In this work, we have illustrated three reaction stages, namely, STAGE(I), STAGE(II), and STAGE(III), and experimentally obtained the oxygen deficiency thresholds of 0.08 and 0.30 for the transition between STAGE(I) and STAGE(II) and STAGE(II) and STAGE(III), respectively.

By using DFT calculations and microkinetic analysis, four active ensembles on $LaFeO_{3-\delta}$ including $Fe-O_5$ (ferryl O), $Fe-O_5$, $Fe-O_4(V_O)$, and $Fe-O_3(V_O)_2$, which correspond to the surface oxygen deficiencies of 0, 0, 0.167, and 0.333 and the Fe-O coordination numbers of 6, 5, 4, and 3,

respectively, were constructed to predict the main active ensembles at the three reaction stages. At the beginning of the reaction, oxygen is highly available on the surface and Fe is in a $Fe-O_5$ (ferryl O) or a $Fe-O_5$ coordination environment, and methane is fully combusted. When the surface oxygen coverage decreases, the partial oxidation of methane to form CO and H_2 takes place at the $Fe-O_4(V_O)$ ensemble. When the concentration of surface oxygen becomes limited and Fe is further reduced to have a $Fe-O_3(V_O)_2$ coordination environment, methane could be decomposed into carbon and H_2 . The pathways for the total combustion and partial oxidation of methane and carbon deposition at different ensembles having different Fe coordination environments, together with a possible relationship between the available surface oxygen and the reaction products, are summarized in Scheme 2.

Upon methane adsorption at the $Fe-O_5$ (ferryl O) ensemble, one of the C-H bonds is broken, leaving CH_3 and H bonded to the oxide surface. The reaction intermediates would be oxidized at the limited $Fe-O_5$ (ferryl O) ensemble to form CO_2 and H_2O . It helps to explain that the fast methane total combustion reaction at the beginning of the reaction on the fresh catalyst. After the ferryl O is consumed, the total combustion and partial oxidation of methane become competing, but the 12% CO selectivity



Scheme 2. Proposed Reaction Mechanism for Methane Oxidation on $LaFeO_3$. The dominant reaction pathway at each ensemble is highlighted with solid lines.

shows the total combustion of methane dominates the overall kinetics at the Fe-O₅ ensemble. Thus, at the beginning of the reaction [STAGE(I)], it turns out that the local structure around Fe on the LaFeO₃ perovskite is likely to have a Fe-O₅ or a Fe-O₅(ferryl O) coordination environment, giving rise to CO₂ production. Meanwhile, the oxygen concentration gradient between bulk and surface is not sufficient to replenish the surface active oxygen sites, which explains the short period at the initial stage at which CO₂ is formed on the fully oxidized catalyst.

At the Fe-O₄(V_O) ensemble, the partial oxidation and total combustion of methane are also two competing parallel reactions. Our microkinetic analysis indicates that fully selective methane oxidation takes place at the Fe-O₄(V_O) ensemble with a CO selectivity of 99%, in striking accord with the experimental observation (98% in the CO selectivity) during most of the course of the reaction where the rate of oxygen diffusion and the surface oxygen consumption rate are almost equal. In other words, the presence of the Fe-O₄(V_O) ensemble involving an oxygen vacancy on the LaFeO₃ surface accounts for the almost 100% CO selectivity obtained experimentally at STAGE(II). Furthermore, by calculating the degree of rate control [88], we found that at the Fe-O₅ ensemble the activation of methane is the rate-limiting step while at the Fe-O₄(V_O) ensemble the dissociation of CH₃ governs the overall rate of the reaction.

Finally, it is found that the methane is decomposed to carbon and H₂ at the Fe-O₃(V_O)₂ ensemble, leading to the initial stage of catalyst deactivation [STAGE(III)] where the bulk oxygen concentration is limited. Both the experimental and theoretical results demonstrate that the reaction pathway depends strongly on the number of O coordinated to Fe [16]. A fully oxidized perovskites result in some CO₂ and H₂O production but these products could be eliminated using a partially oxidized perovskites during the reduction process. Therefore, the active ensembles where the Fe cations are in different coordination environments in the reaction are believed to be of central importance in the activation of methane and product distribution, and fully selective methane partial oxidation can be achieved by precisely controlling the oxidation time (and hence the amount of oxygen injected into the perovskite), independent of the catalyst material used.

4. Conclusions

In this contribution, a combined experimental and theoretical study has been carried out to reveal the dynamic nature of active sites on the La-Fe-based perovskites for chemical looping methane oxidation. It is found that the reduction reaction of the catalyst can be divided into three stages, which could take place at four different active ensembles that have four types of Fe coordination environments. The oxygen deficiency thresholds of 0.08 and 0.30 for the transition between STAGE (I) and STAGE(II) and STAGE(II) and STAGE(III), respectively, are obtained experimentally. At STAGE(I), the total combustion of methane dominates the overall kinetics on the catalyst surface where Fe is likely to have a Fe-O₅ or a Fe-O₅(ferryl O) coordination environment and the main oxidation products are CO₂ as well as H₂O. At STAGE(II) which is the major part of the reaction, the Fe-O₄(V_O) ensemble involving an oxygen vacancy is predicted to lead to fully selective methane conversion to CO (99% in the CO selectivity), in striking accord with the experimentally observed CO selectivity of 98%. Hence, at this reaction stage, the catalyst surface is most likely to be oxygen-deficient, which also explains why the partially oxidized LaFeO₃ perovskite gives rise to a high CO selectivity. At STAGE(III), carbon deposition would take place at the Fe-O₃(V_O)₂ ensemble having two neighboring oxygen vacancies, leading to the initial stage of deactivation of the catalyst.

Our results illustrate that lattice oxygen participates in the redox reaction by the Mars van Krevelen mechanism. CO₂ proves to be the primary product of methane oxidation rather than a secondary product of CO oxidation. The presence of surface oxygen vacancies would dramatically increase the overall energy barrier for total oxidation, thus decreasing the selectivity toward CO₂. Hence, the Fe coordination

environment (and hence the surface oxygen vacancy concentration) is the key factor governing the catalyst selectivity. The methane oxidation reaction may vary from total combustion on the O-rich surface to fully selective partial oxidation on the O-deficient surface. In light of these facts, we propose a strategy of controlling the oxidation time of perovskites for a desired oxygen vacancy concentration in bulk oxide, which proves particularly useful for designing highly selective catalysts for methane partial oxidation.

CRedit authorship contribution statement

Jie Yang: Investigation; Writing – original draft. **Erlend Bjørgum:** Investigation. **Hui Chang:** Investigation; Writing – original draft. **Ka-Ke Zhu:** Formal analysis. **Zhi-Jun Sui:** Software; Validation. **Xing-Gui Zhou:** Supervision, **Anders Holmen:** Resources. **Yi-An Zhu:** Project administration; Writing – review & editing. **De Chen:** Project administration; Writing – review & editing.

Declaration of Competing Interest

The authors declare that they have no known competing financial interests or personal relationships that could have appeared to influence the work reported in this paper.

Acknowledgement

This work is supported by the Natural Science Foundation of China (21473053, 22073027, and 22178111), the Natural Science Foundation of Shanghai (20ZR1415800), the Fundamental Research Funds for the Central Universities (222201718003), and the Norwegian Research Council through the KOSK program. The computational time provided by the Notur project is highly acknowledged.

Appendix A. Supporting information

Supplementary data associated with this article can be found in the online version at doi:10.1016/j.apcatb.2021.120788.

References

- [1] T.V. Choudhary, V.R. Choudhary, Energy-efficient syngas production through catalytic oxy-methane reforming reactions, *Angew. Chem. Int. Ed.* 47 (2008) 1828–1847.
- [2] M. Rydén, A. Lyngfelt, T. Mattisson, D. Chen, A. Holmen, E. Bjørgum, Novel oxygen-carrier materials for chemical-looping combustion and chemical-looping reforming: La_xSr_{1-x}Fe_yCo_{1-y}O_{3-δ} perovskites and mixed-metal oxides of NiO, Fe₂O₃ and Mn₂O₄, *Int. J. Greenh. Gas Control* 2 (2008) 21–36.
- [3] F. He, Y.-G. Wei, H.-B. Li, H. Wang, Synthesis gas generation by chemical-looping reforming using Ce-based oxygen carriers modified with Fe, Cu, and Mn oxides, *Energy Fuel* 23 (2009) 2095–2102.
- [4] L.-S. Fan, L. Zeng, S. Luo, Chemical-looping technology platform, *AlChE J.* 61 (2015) 2–22.
- [5] P. Mars, D.W. van Krevelen, Oxidations carried out by means of vanadium oxide catalysts, *Chem. Eng. Sci.* 3 (1954) 41–59.
- [6] E.R. Stobbe, B.A. de Boer, J.W. Geus, The reduction and oxidation behaviour of manganese oxides, *Catal. Today* 47 (1999) 161–167.
- [7] K. Otsuka, T. Ushiyama, I. Yamanaka, Partial oxidation of methane using the redox of cerium oxide, *Chem. Lett.* 22 (1993) 1517–1520.
- [8] M. Funabiki, T. Yamada, K. Kayano, Auto exhaust catalysts, *Catal. Today* 10 (1991) 33–43.
- [9] M.Vd Bossche, H. Grönbeck, Methane oxidation over PdO(101) revealed by first-principles kinetic modeling, *J. Am. Chem. Soc.* 137 (2015) 12035–12044.
- [10] E. Jernald, T. Mattisson, A. Lyngfelt, Thermal analysis of chemical-looping combustion, *Chem. Eng. Res. Des.* 84 (2006) 795–806.
- [11] L. Zeng, Z. Cheng, J.A. Fan, L.-S. Fan, J.-L. Gong, Metal oxide redox chemistry for chemical looping processes, *Nat. Rev. Chem.* 2 (2018) 349–364.
- [12] Y.-G. Jin, C.-H. Sun, S. Su, Experimental and theoretical study of the oxidation of ventilation air methane over Fe₂O₃ and CuO, *Phys. Chem. Chem. Phys.* 17 (2015) 16277–16284.
- [13] Y.C. Li Ranjia, Dai Xiaoping, Shen Shikong, Partial oxidation of methane to synthesis gas using lattice oxygen instead of molecular oxygen, *Chin. J. Catal.* 23 (2002) 381–387.
- [14] Å. Slagtern, U. Olsbye, Partial oxidation of methane to synthesis gas using La-M-O catalysts, *Appl. Catal. A* 110 (1994) 99–108.

- [15] F.S. Toniolo, R.N.S.H. Magalhães, C.A.C. Perez, M. Schmal, Structural investigation of LaCoO_3 and LaCoCuO_3 perovskite-type oxides and the effect of Cu on coke deposition in the partial oxidation of methane, *Appl. Catal. B Environ.* 117–118 (2012) 156–166.
- [16] O. Mihai, D. Chen, A. Holmen, Chemical looping methane partial oxidation: the effect of the crystal size and O content of LaFeO_3 , *J. Catal.* 293 (2012) 175–185.
- [17] M.A. Peña, J.L.G. Fierro, Chemical structures and performance of perovskite oxides, *Chem. Rev.* 101 (2001) 1981–2018.
- [18] S.B. Adler, Factors governing oxygen reduction in solid oxide fuel cell cathodes, *Chem. Rev.* 104 (2004) 4791–4844.
- [19] J. Suntivich, H.A. Gasteiger, N. Yabuuchi, H. Nakanishi, J.B. Goodenough, Y. Shao-Horn, Design principles for oxygen-reduction activity on perovskite oxide catalysts for fuel cells and metal–air batteries, *Nat. Chem.* 3 (2011) 546–550.
- [20] S. Royer, D. Duprez, F. Can, X. Courtois, C. Batiot-Dupeyrat, S. Laassiri, H. Alamdari, Perovskites as substitutes of noble metals for heterogeneous catalysis: dream or reality, *Chem. Rev.* 114 (2014) 10292–10368.
- [21] K.A. Stoerzinger, R. Comes, S.R. Spurgeon, S. Thevuthasan, K. Ihm, E.J. Crumlin, S. A. Chambers, Influence of LaFeO_3 surface termination on water reactivity, *J. Phys. Chem. Lett.* 8 (2017) 1038–1043.
- [22] H. Wang, C. Tablet, A. Feldhoff, J. Caro, A cobalt-free oxygen-permeable membrane based on the perovskite-type oxide $\text{Ba}_{0.5}\text{Sr}_{0.5}\text{Zn}_{0.2}\text{Fe}_{0.8}\text{O}_{3-\delta}$, *Adv. Mater.* 17 (2005) 1785–1788.
- [23] J.W. Fergus, Perovskite oxides for semiconductor-based gas sensors, *Sens. Actuators B-Chem.* 123 (2007) 1169–1179.
- [24] R. Spinicci, M. Faticanti, P. Marini, S. De Rossi, P. Porta, Catalytic activity of LaMnO_3 and LaCoO_3 perovskites towards VOCs combustion, *J. Mol. Catal. A: Chem.* 197 (2003) 147–155.
- [25] L.V. Yafarova, I.V. Chislova, I.A. Zvereva, T.A. Kryuchkova, V.V. Kost, T. F. Sheshko, Sol–gel synthesis and investigation of catalysts on the basis of perovskite-type oxides GdMO_3 ($M = \text{Fe}, \text{Co}$), *J. Sol. -Gel. Sci. Technol.* 92 (2019) 264–272.
- [26] X. Yin, S. Wang, B. Wang, L. Shen, Perovskite-type $\text{LaMn}_{1-x}\text{B}_x\text{O}_{3+\delta}$ ($B = \text{Fe}, \text{Co}$ and Ni) as oxygen carriers for chemical looping steam methane reforming, *Chem. Eng. J.* 422 (2021), 128751.
- [27] X. Zhang, C. Pei, X. Chang, S. Chen, R. Liu, Z.-J. Zhao, R. Mu, J. Gong, FeO_6 octahedral distortion activates lattice oxygen in perovskite ferrite for methane partial oxidation coupled with CO_2 splitting, *J. Am. Chem. Soc.* 142 (2020) 11540–11549.
- [28] L. Zhang, W. Xu, J. Wu, Y. Hu, C. Huang, Y. Zhu, M. Tian, Y. Kang, X. Pan, Y. Su, J. Wang, X. Wang, Identifying the role of A-site cations in modulating oxygen capacity of iron-based perovskite for enhanced chemical looping methane-to-syngas conversion, *ACS Catal.* 55 (2020) 9420–9430.
- [29] F. Donat, C.R. Müller, CO_2 -free conversion of CH_4 to syngas using chemical looping, *Appl. Catal. B Environ.* 278 (2020), 119328.
- [30] H. Chang, E. Bjørgum, O. Mihai, J. Yang, H.L. Lein, T. Grande, S. Raaen, Y.-A. Zhu, A. Holmen, D. Chen, Effects of oxygen mobility in La–Fe-based perovskites on the catalytic activity and selectivity of methane oxidation, *ACS Catal.* 10 (2020) 3707–3719.
- [31] Y. Zheng, K. Li, H. Wang, D. Tian, Y. Wang, X. Zhu, Y. Wei, M. Zheng, Y. Luo, Designed oxygen carriers from macroporous LaFeO_3 supported CeO_2 for chemical-looping reforming of methane, *Appl. Catal. B Environ.* 202 (2017) 51–63.
- [32] X. Dai, J. Cheng, Z. Li, M. Liu, Y. Ma, X. Zhang, Reduction kinetics of lanthanum ferrite perovskite for the production of synthesis gas by chemical-looping methane reforming, *Chem. Eng. Sci.* 153 (2016) 236–245.
- [33] X.P. Dai, J. Li, J.T. Fan, W.S. Wei, J. Xu, Synthesis gas generation by chemical-looping reforming in a circulating fluidized bed reactor using perovskite LaFeO_3 -based oxygen carriers, *Ind. Eng. Chem. Res.* 51 (2012) 11072–11082.
- [34] X. Dai, C. Yu, Q. Wu, Comparison of LaFeO_3 , $\text{La}_{0.8}\text{Sr}_{0.2}\text{FeO}_3$, and $\text{La}_{0.8}\text{Sr}_{0.2}\text{Fe}_{0.9}\text{Co}_{0.1}\text{O}_3$ perovskite oxides as oxygen carrier for partial oxidation of methane, *J. Nat. Gas. Chem.* 17 (2008) 415–418.
- [35] X.P. Dai, Q. Wu, R.J. Li, C.C. Yu, Z.P. Hao, Hydrogen production from a combination of the water–gas shift and redox cycle process of methane partial oxidation via lattice oxygen over LaFeO_3 perovskite catalyst, *J. Phys. Chem. B* 110 (2006) 25856–25862.
- [36] X.P. Dai, R.J. Li, C.C. Yu, Z.P. Hao, Unsteady-state direct partial oxidation of methane to synthesis gas in a fixed-bed reactor using AFeO_3 ($A = \text{La}, \text{Nd}, \text{Eu}$) perovskite-type oxides as oxygen storage, *J. Phys. Chem. B* 110 (2006) 22525–22531.
- [37] X. Zhang, C. Pei, X. Chang, S. Chen, R. Liu, Z.-J. Zhao, R. Mu, J. Gong, FeO_6 octahedral distortion activates lattice oxygen in perovskite ferrite for methane partial oxidation coupled with CO_2 splitting, *J. Am. Chem. Soc.* 142 (2020) 11540–11549.
- [38] O. Mihai, D. Chen, A. Holmen, Catalytic consequence of oxygen of lanthanum ferrite perovskite in chemical looping reforming of methane, *Ind. Eng. Chem. Res.* 50 (2011) 2613–2621.
- [39] J.-J. Tang, B. Liu, Reactivity of the Fe_2O_3 (0001) surface for methane oxidation: a GGA + U study, *J. Phys. Chem. C* 120 (2016) 6642–6650.
- [40] L. Huang, M.-C. Tang, M.-H. Fan, H.-S. Cheng, Density functional theory study on the reaction between hematite and methane during chemical looping process, *Appl. Energy* 159 (2015) 132–144.
- [41] Q. Shen, F. Huang, M. Tian, Y. Zhu, L. Li, J. Wang, X. Wang, Effect of regeneration period on the selectivity of synthesis gas of Ba-hexaaluminates in chemical looping partial oxidation of methane, *ACS Catal.* 9 (2019) 722–731.
- [42] Z. Cheng, L. Qin, M.-Q. Guo, M.-Y. Xu, J.A. Fan, L.-S. Fan, Oxygen vacancy promoted methane partial oxidation over iron oxide oxygen carriers in the chemical looping process, *Phys. Chem. Chem. Phys.* 18 (2016) 32418–32428.
- [43] H.S. Lim, M. Lee, D. Kang, J.W. Lee, Role of transition metal in perovskites for enhancing selectivity of methane to syngas, *Int. J. Hydrogen Energy* 43 (2018) 20580–20590.
- [44] X. Yin, S. Wang, B. Wang, L. Shen, Perovskite-type $\text{LaMn}_{1-x}\text{B}_x\text{O}_{3+\delta}$ ($B = \text{Fe}, \text{Co}$ and Ni) as oxygen carriers for chemical looping steam methane reforming, *Chem. Eng. J.* 422 (2021), 128751.
- [45] Y. Liu, L. Qin, Z. Cheng, J.W. Goetze, F. Kong, J.A. Fan, L.-S. Fan, Near 100% CO selectivity in nanoscaled iron-based oxygen carriers for chemical looping methane partial oxidation, *Nat. Commun.* 10 (2019) 5503.
- [46] L.A. Chick, L.R. Pederson, G.D. Maupin, J.L. Bates, L.E. Thomas, G.J. Exarhos, Glycine–nitrate combustion synthesis of oxide ceramic powders, *Mater. Lett.* 10 (1990) 6–12.
- [47] G. Kresse, J. Hafner, Ab initio molecular dynamics for open-shell transition metals, *Phys. Rev. B* 48 (1993) 13115–13118.
- [48] G. Kresse, J. Furthmüller, Efficient iterative schemes for ab initio total-energy calculations using a plane-wave basis set, *Phys. Rev. B* 54 (1996) 11169–11186.
- [49] G. Kresse, J. Furthmüller, Efficiency of ab-initio total energy calculations for metals and semiconductors using a plane-wave basis set, *Comp. Mater. Sci.* 6 (1996) 15–50.
- [50] J. Wellendorff, K.T. Lundgaard, A. Møgelhøj, V. Petzold, D.D. Landis, J.K. Nørskov, T. Bligaard, K.W. Jacobsen, Density functionals for surface science: Exchange-correlation model development with Bayesian error estimation, *Phys. Rev. B* 85 (2012), 235149.
- [51] G. Kresse, D. Joubert, From ultrasoft pseudopotentials to the projector augmented-wave method, *Phys. Rev. B* 59 (1999) 1758–1775.
- [52] A.J. Cohen, P. Mori-Sánchez, W. Yang, Insights into current limitations of density functional theory, *Science* 321 (2008) 792–794.
- [53] V.I. Anisimov, F. Aryasetiawan, A.I. Lichtenstein, First-principles calculations of the electronic structure and spectra of strongly correlated systems: the LDA+U method, *J. Phys.: Condens. Matter* 9 (1997) 767–808.
- [54] V.I. Anisimov, J. Zaanen, O.K. Andersen, Band theory and Mott insulators: Hubbard U instead of Stoner I, *Phys. Rev. B* 44 (1991) 943–954.
- [55] S.L. Dudarev, G.A. Botton, S.Y. Savrasov, C.J. Humphreys, A.P. Sutton, Electron-energy-loss spectra and the structural stability of nickel oxide: An LSDA+U study, *Phys. Rev. B* 57 (1998) 1505–1509.
- [56] Y. Li, Y.-S. Zheng, Y.-A. Zhu, Z.-J. Sui, X.-G. Zhou, D. Chen, W.-K. Yuan, BEEF-vdW + U method applied to perovskites: thermodynamic, structural, electronic, and magnetic properties, *J. Phys.: Condens. Matter* 31 (2019), 145901.
- [57] H.J. Monkhorst, J.D. Pack, Special points for Brillouin-zone integrations, *Phys. Rev. B* 13 (1976) 5188–5192.
- [58] G. Henkelman, H. Jónsson, A dimer method for finding saddle points on high dimensional potential surfaces using only first derivatives, *J. Chem. Phys.* 111 (1999) 7010–7022.
- [59] Q. Li, Y.-X. Deng, Y.-A. Zhu, Y. Li, Z.-J. Sui, D. Chen, W.-K. Yuan, Structural stability of Lanthanum-based oxygen-deficient perovskites in redox catalysis: a density functional theory study, *Catal. Today* (2018).
- [60] Y. Li, J. Yang, Y.-A. Zhu, Z.-J. Sui, X.-G. Zhou, D. Chen, W.-K. Yuan, Surface phase diagrams of La-based perovskites towards the O-rich limit from first principles, *Phys. Chem. Chem. Phys.* 21 (2019) 12859–12871.
- [61] Y.A. Mastrikov, R. Merkle, E.A. Kotomin, Maija M. Kuklja, J. Maier, Surface termination effects on the oxygen reduction reaction rate at fuel cell cathodes, *J. Mater. Chem. A* 6 (2018) 11929–11940.
- [62] Y.A. Mastrikov, R. Merkle, E. Heifets, E.A. Kotomin, J. Maier, Pathways for oxygen incorporation in mixed conducting perovskites: a DFT-based mechanistic analysis for $(\text{La}, \text{Sr})\text{MnO}_{3-\delta}$, *J. Phys. Chem. C* 114 (2010) 3017–3027.
- [63] V. Fung, F. Polo-Garzon, Z. Wu, D.-E. Jiang, Exploring perovskites for methane activation from first principles, *Catal. Sci. Technol.* 8 (2018) 702–709.
- [64] X. Rong, J. Parolin, A.M. Kolpak, A fundamental relationship between reaction mechanism and stability in metal oxide catalysts for oxygen evolution, *ACS Catal.* 6 (2016) 1153–1158.
- [65] F. Polo-Garzon, S.-Z. Yang, V. Fung, G.S. Foo, E.E. Bickel, M.F. Chisholm, D.-E. Jiang, Z. Wu, Controlling reaction selectivity through the surface termination of perovskite, *Catal., Angew. Chem. Int. Ed.* 56 (2017) 9820–9824.
- [66] Q. Li, Q. Yin, Y.-S. Zheng, Z.-J. Sui, X.-G. Zhou, D. Chen, Y.-A. Zhu, Insights into hydrogen transport behavior on perovskite surfaces: transition from the Grothuss mechanism to the vehicle mechanism, *Langmuir* 35 (2019) 9962–9969.
- [67] M.M. Arman, N.G. Imam, R. Loreda Portales, S.I. El-Dek, Synchrotron radiation X-ray absorption fine structure and magnetization improvement of A-site Ce^{3+} doped LaFeO_3 , *J. Magn. Magn. Mater.* 513 (2020), 167097.
- [68] A. Deb, J.M. Ralph, E.J. Cairns, U. Bergmann, Characterization of $\text{La}_{0.8}\text{Sr}_{0.2}\text{FeO}_{3-\delta}$ and $\text{La}_{0.7}\text{Sr}_{0.2}\text{FeO}_{3-\delta}$ as a function of temperature by x-ray absorption spectroscopy, *Phys. Rev. B* 73 (2006), 115114.
- [69] A.J. Medford, C. Shi, M.J. Hoffmann, A.C. Lausche, S.R. Fitzgibbon, T. Bligaard, J. K. Nørskov, CatMAP: a software package for descriptor-based microkinetic mapping of catalytic, *Trends Catal.* 145 (2015) 794–807.
- [70] L. Xiao, Y.-L. Shan, Z.-J. Sui, D. Chen, X.-G. Zhou, W.-K. Yuan, Y.-A. Zhu, Beyond the reverse Horiuti–Polanyi mechanism in propane dehydrogenation over Pt catalysts, *ACS Catal.* 10 (2020) 14887–14902.
- [71] X. Zhu, K.-Z. Li, L. Neal, F.-X. Li, Perovskites as geo-inspired oxygen storage materials for chemical looping and three-way catalysis: a perspective, *ACS Catal.* 8 (2018) 8213–8236.
- [72] Q. Li, Y.-X. Deng, Y.-A. Zhu, Y. Li, Z.-J. Sui, D. Chen, W.-K. Yuan, Structural stability of lanthanum-based oxygen-deficient perovskites in redox catalysis: a density functional theory study, *Catal. Today* 347 (2020) 142–149.
- [73] J.N. Bronsted, Acid and basic catalysis, *Chem. Rev.* 5 (1928) 231–338.

- [74] M.G. Evans, M. Polanyi, Further considerations on the thermodynamics of chemical equilibria and reaction rates, *Trans. Faraday Soc.* 32 (1936) 1333–1360.
- [75] Y. Li, W. Cheng, Z.-J. Sui, X.-G. Zhou, D. Chen, W.-K. Yuan, Y.-A. Zhu, Origin of chemisorption energy scaling relations over perovskite surfaces, *J. Phys. Chem. C* 123 (2019) 28275–28283.
- [76] J.H. Montoya, A.D. Doyle, J.K. Nørskov, A. Vojvodic, Trends in adsorption of electrocatalytic water splitting intermediates on cubic ABO₃ oxides, *Phys. Chem. Chem. Phys.* 20 (2018) 3813–3818.
- [77] F. Abild-Pedersen, J. Greeley, F. Studt, J. Rossmeisl, T.R. Munter, P.G. Moses, E. Skúlason, T. Bligaard, J.K. Nørskov, Scaling properties of adsorption energies for hydrogen-containing molecules on transition-metal surfaces, *Phys. Rev. Lett.* 99 (2007), 016105.
- [78] Y.-H. Chin, C. Buda, M. Neurock, E. Iglesia, Consequences of metal–oxide interconversion for C–H bond activation during CH₄ reactions on Pd catalysts, *J. Am. Chem. Soc.* 135 (2013) 15425–15442.
- [79] Y.-A. Zhu, Y.-C. Dai, D. Chen, W.-K. Yuan, First-principles calculations of CH₄ dissociation on Ni(100) surface along different reaction pathways, *J. Mol. Catal. A: Chem.* 264 (2007) 299–308.
- [80] V.I. Lomonosov, M.Y. Sinev, Oxidative coupling of methane: mechanism and kinetics, *Kinet. Catal.* 57 (2016) 647–676.
- [81] W.-D. Hu, J.-G. Lan, Y. Guo, X.-M. Cao, P. Hu, Origin of efficient catalytic combustion of Methane over Co₃O₄(110): active low-coordination lattice oxygen and cooperation of multiple active sites, *ACS Catal.* 6 (2016) 5508–5519.
- [82] Y. Wang, X. Yang, L. Hu, Y. Li, J. Li, Theoretical study of the crystal plane effect and ion-pair active center for C–H bond activation by Co₃O₄ nanocrystals, *Chin. J. Catal.* 35 (2014) 462–467.
- [83] F. Lin, S.-Y. Wang, F.-W. Zheng, G. Zhou, J. Wu, B.-L. Gu, W.-H. Duan, Hydrogen-induced metallicity of SrTiO₃(001) surfaces: a density functional theory study, *Phys. Rev. B* 79 (2009), 035311-51.
- [84] Y. Zeng, S. Tamhankar, N. Ramprasad, F. Fitch, D. Acharya, R. Wolf, A novel cyclic process for synthesis gas production, *Chem. Eng. Sci.* 58 (2003) 577–582.
- [85] Y. Zeng, Y.S. Lin, A transient TGA study on oxygen permeation properties of perovskite-type ceramic membrane, *Solid State Ion.* 110 (1998) 209–221.
- [86] M. Fathi, E. Bjorgum, T. Viig, O.A. Rokstad, Partial oxidation of methane to synthesis gas: elimination of gas phase oxygen, *Catal. Today* 63 (2000) 489–497.
- [87] M. Fathi, E. Bjorgum, O.A. Rokstad, Conversion of ethane to ethylene and synthesis gas with cerium oxide. Promoting effect of Pt, Rh and Ru, *Catal. Lett.* 72 (2001) 25–31.
- [88] C. Stegelmann, A. Andreasen, C.T. Campbell, Degree of rate control: how much the energies of intermediates and transition states control rates, *J. Am. Chem. Soc.* 131 (2009) 8077–8082.